A Novel SAGE Algorithm for Estimating Parameters of Wideband Spatial Nonstationary Wireless Channels With Antenna Polarization

Zihao Zhou, *Student Member, IEEE*, Cheng-Xiang Wang, *Fellow, IEEE*, Li Zhang, *Student Member, IEEE*, Jie Huang, *Member, IEEE*, Lijian Xin, *Member, IEEE*, El-Hadi M. Aggoune, *Life Senior Member, IEEE*, and Yang Miao, *Member, IEEE*

Abstract— In this article, a novel space-alternating generalized expectation–maximization (SAGE) algorithm is proposed for parameter estimations of wideband spatial nonstationary wireless channels with antenna polarization (SAGE-WSNSAP). Compared with the traditional SAGE algorithm, the proposed SAGE-WSNSAP algorithm adds spatial nonstationarity by introducing birth–death coefficients at both transmitter (Tx) and receiver (Rx) sides into the parametric model. To reduce the complexity of the SAGE-WSNSAP algorithm, a coarse-to-fine search method is adopted in the initialization step. In addition, multiple-input multiple-output (MIMO) channel measurements are conducted to validate the proposed algorithm. The measurement results of the angle-delay power spectral density (PSD) and average delay PSD are compared with those estimated by the far-field SAGE algorithm, the near-field SAGE algorithm, and the proposed algorithm. It is found that the estimation results using the proposed SAGE-WSNSAP algorithm show higher similarity to measurement results than using the other two SAGE algorithms. In comparison to the far-field and near-field SAGE algorithms, the SAGE-WSNSAP algorithm can extract more effective multipath components (MPCs) and improve the power extraction ratios.

Index Terms— Antenna polarization, channel parameter estimation, space-alternating generalized expectation–maximization (SAGE), spatial nonstationarity, wideband.

I. INTRODUCTION

BEYOND fifth generation (5G) and sixth generation (6G), wireless communications have introduced some key technologies [1], [2], e.g., millimeter-wave (mmWave), massive multiple-input multiple-output (MIMO) [3], and integrated sensing and communication (ISAC) [4], [5], [6]. The mmWave band has the advantage of wide spectrum bandwidth, thereby greatly improving the capacity of communication systems. However, the mmWave bands lead to larger path loss compared with the sub-6 GHz frequency bands [7]. The mm-scale wavelength makes it feasible to encapsulate numerous antennas over a small area to form a large antenna array [8]. Therefore, the beamforming technology can be applied to increase the beam gain to compensate for the high path loss [9], [10]. In ISAC, sensing and communication are integrated into a system that can actively sense the surrounding physical environment to improve the communication performance [11]. In addition, massive MIMO and mmWave are able to improve angular and delay resolution for ISAC, thereby improving perception and localization accuracy [12]. As the basis of wireless communication systems' design, channel models that can accurately describe these new application scenarios are very important. Channel measurements are essential for establishing accurate channel models. To process the measured data, channel parameter estimation (CPE) algorithms have been widely studied to extract multipath components (MPCs) information, e.g., amplitude, delay, and angle. These parameters are of great importance to establish a realistic channel model. Therefore, the accuracy of CPE algorithms is crucial for evaluating communication or sensing performance.

However, channel characteristics in beyond 5G and 6G application scenarios bring challenges to CPE algorithms, where the following channel characteristics need to be carefully considered. The narrowband assumption [13] commonly used in the traditional CPE algorithms may not be satisfied due to the large bandwidth. It means that due to the large

bandwidth increasing the delay resolution, the delay of the same MPC reaching different antenna elements is distributed in different delay bins. As the number of antennas increases, forming a massive MIMO system, the spherical wavefront (i.e., near-field) can be observed [14]. At this time, the plane wavefront assumption (i.e., far-field) can lead to the mismatch between the parametric model and measurement results, resulting in estimation error or even estimation failure [15]. Another important channel characteristic is the antenna polarization, which is described by co-polarization and cross-polarization components. In [16], a polarized MIMO channel model was presented based on the geometric channel depolarization method, which well agreed with polarization channel measurements. The investigation in [17] has demonstrated that only considering the single-polarization characteristics of the antenna can lead to serious estimation errors. In addition, numerous measurements show that massive MIMO channels exhibit obvious spatial nonstationarity. The appearance and disappearance of MPCs were observed along the antenna array [18], [19], [20]. To accurately extract channel parameters, it is of great importance to establish a CPE algorithm that can simultaneously consider all the above channel characteristics.

Generally, the CPE algorithms can be divided into three categories [21], i.e., spectral-based method, parametric subspace-based method, and maximum-likelihood (ML)-based method. The Bartlett spectrum [22] and Capon spectrum [23] are two commonly used spectral-based estimation algorithms. These algorithms are suitable for real-time parameter estimation and have a low complexity [13], but the spectral resolution is relatively low. The parametric subspace-based algorithms, such as unitary estimation of signal parameter via rotational invariance techniques (ESPRIT) [24] and multiple signal classification (MUSIC) [25], were based on narrowband far-field assumptions. In [26] and [27], the characteristic was added to the MUSIC algorithm by introducing near-field scatterers. However, the large bandwidth and spatial nonstationary characteristics are still missing. The ML-based estimation algorithms, e.g., Richter's ML estimation (RiMAX) [28] and expectation maximization (EM) [29], are characterized by high resolution and high complexity. In [15], an algorithm based on the EM principle was proposed to estimate wideband 3-D near-field channel parameters. However, channel characteristics of antenna polarization and spatial nonstationarity were not considered in this algorithm. Besides, as an extension of the EM algorithm, the space-alternating generalized expectation–maximization (SAGE) algorithm [30] can significantly reduce the complexity by dividing channel parameters into multiple subsets. In [31], the SAGE algorithm was further used to locate the position of scatterers based on the narrowband near-field model. Although the spatial nonstationarity has been incorporated in some channel models [32], [33], this channel characteristic has not been thoroughly considered in CPE algorithms. In [34] and [35], a trajectory-aided high-resolution parameter estimation (HRPE) algorithm was proposed, which took advantage of the large bandwidth for MPCs' delay trajectories' identification. The breakpoints in the MPC's delay trajectory were considered as the positions where the MPC disappeared. However, this algorithm only supports large antenna array at one side and cannot be applied to a polarization antenna array.

In summary, most CPE algorithms mentioned above were based on narrowband and far-field assumptions [22], [23], [24], [25], [28], [30]. In [26], [27], and [31], the near-field characteristic was considered, and the near-field and wideband characteristics were considered in [15]. In [34] and [35], the channel characteristics of near-field, wideband, and spatial nonstationarity were considered in the parametric model, but the antenna polarization was ignored. To the best of the authors' knowledge, there is no CPE algorithm that can simultaneously incorporate the channel characteristics of near-field, wideband, antenna polarization, and spatial nonstationarity. To fill the research gaps, a novel SAGE algorithm for parameter estimations of wideband spatial nonstationary wireless channels with antenna polarization (SAGE-WSNSAP) is proposed. In addition, it is comprehensively compared with the conventional far-field and near-field SAGE algorithms to show its advantages and effectiveness by channel measurements. The main contributions and novelties of this article are as follows.

1) The proposed SAGE-WSNSAP algorithm can simultaneously support important channel characteristics, including near-field, wideband, antenna polarization, and spatial nonstationarity. Besides, a coarse-to-fine search method is adopted in the proposed algorithm to reduce the computational complexity.

2) Channel measurements with 64×32 dual-polarization massive MIMO antenna array are conducted in a typical indoor office scenario. The spatial nonstationarity can be clearly observed at the receiver (Rx) side. Furthermore, the measurement data are used to validate the proposed algorithm.

3) The MPCs' parameter estimation performance based on the SAGE-WSNSAP algorithm is compared with that based on the far-field and near-field SAGE algorithms, including the angle-delay power spectral density (PSD) and the average delay PSD. Besides, the power extraction ratios of these algorithms in both the line-of-sight (LOS) and non-LOS (NLOS) scenarios are calculated and compared.

The rest of this article is organized as follows. Section II presents the spatial nonstationary signal model. In Section III, the principle and detailed steps of the SAGE-WSNSAP algorithm are presented. Then, Section IV introduces the specific system configuration and channel measurements. Section V shows the performance of the SAGE-WSNSAP algorithm, far-field SAGE algorithm, and near-field SAGE algorithm. Finally, conclusions are drawn in Section VI.

II. Spatial Nonstationary Signal Model

Before introducing the proposed SAGE-WSNSAP algorithm, this section first presents three signal models, which will be used in the proposed algorithm in Section III.

A. Narrowband Far-Field Signal Model With Antenna Polarization

In the traditional MIMO signal model, it is assumed that the electromagnetic wave propagation conforms to the plane

wavefront, which is also known as the far-field assumption [30]. Under this assumption, the MPC shows the same angle of arrival (AoA) to all the antennas at the Rx side, and similarly, the angle of departure (AoD) of the MPC to all the antennas at the transmitter (Tx) side is identical. Besides, the delay of the MPC observed by all the antenna elements is the same. The Rx antenna array and Tx antenna array are equipped with M and N antennas, respectively. The transfer function of the lth MPC between the mth Rx antenna and the nth Tx antenna $\mathbf{H}_{m,n,l}(\boldsymbol{f}) \in \mathbb{C}^{K \times 1}$ can be expressed as [38]

$$
\begin{aligned}
\mathbf{H}_{m,n,l}(\boldsymbol{f}) = \sum_{P_{\mathrm{Rx}}=1}^{2} \sum_{P_{\mathrm{Tx}}=1}^{2} & \alpha_{l,P_{\mathrm{Rx}},P_{\mathrm{Tx}}} F_{\mathrm{Rx},m,P_{\mathrm{Rx}}}(\boldsymbol{\Omega}_{\mathrm{Rx},l}) \\
& \cdot F_{\mathrm{Tx},n,P_{\mathrm{Tx}}}(\boldsymbol{\Omega}_{\mathrm{Tx},l}) e^{j\frac{2\pi}{\lambda}\langle \boldsymbol{\Omega}_{\mathrm{Rx},l} \cdot \boldsymbol{r}_{\mathrm{Rx},m}\rangle} \\
& \cdot e^{j\frac{2\pi}{\lambda}\langle \boldsymbol{\Omega}_{\mathrm{Tx},l} \cdot \boldsymbol{r}_{\mathrm{Tx},n}\rangle} e^{-j2\pi \boldsymbol{f} \tau_l}
\end{aligned} \tag{1}
$$

where $\boldsymbol{f} = [f_1, \ldots, f_K]^T \in \mathbb{R}^{K \times 1}$ represents the K frequency points, $[\cdot]^T$ denotes the transpose operation, and $\langle \cdot \rangle$ represents the inner product. Here, $\mathbb{C}$ and $\mathbb{R}$ represent the complex numbers' set and real numbers' set, respectively. Besides, $P_{\mathrm{Rx}} \in \{1, 2\}$ and $P_{\mathrm{Tx}} \in \{1, 2\}$ are used to denote two mutually orthogonal polarization modes of antennas at Rx and Tx sides. In addition, $\alpha_{l,P_{\mathrm{Rx}},P_{\mathrm{Tx}}}$ represents the complex attenuation of the lth MPC undergoing P_{Rx}-polarization and P_{Tx}-polarization. The complex gain of P_{Tx}-polarization of the nth Tx antenna in direction $\boldsymbol{\Omega}_{\mathrm{Tx},l}$ is denoted by $F_{\mathrm{Tx},n,P_{\mathrm{Tx}}}(\boldsymbol{\Omega}_{\mathrm{Tx},l})$, and $F_{\mathrm{Rx},m,P_{\mathrm{Rx}}}(\boldsymbol{\Omega}_{\mathrm{Rx},l})$ represents P_{Rx}-polarization of the mth Rx antenna in direction $\boldsymbol{\Omega}_{\mathrm{Rx},l}$. Moreover, $\boldsymbol{\Omega}_{\mathrm{Tx},l}$, $\boldsymbol{\Omega}_{\mathrm{Rx},l}$, and τ_l represent the AoD, AoA, and delay of the lth MPC, respectively. The position vectors of the nth Tx antenna and mth Rx antenna are denoted by $\boldsymbol{r}_{\mathrm{Tx},n}$ and $\boldsymbol{r}_{\mathrm{Rx},m}$, respectively.

The direction vector $\boldsymbol{\Omega}$ is a unit vector, which can be calculated by the azimuth angle ϕ and the elevation angle θ as [31]

$$
\boldsymbol{\Omega} = [\cos\phi\cos\theta, \cos\phi\sin\theta, \sin\theta \ ]^T. \tag{2}
$$

B. Wideband Near-Field Signal Model With Antenna Polarization

As the number of antennas increases, the Rayleigh distance of the antenna array also increases. The Rayleigh distance can be calculated by $d_{\mathrm{Rayleigh}} = 2D^2/\lambda$, where D and λ denote the antenna array aperture and wavelength, respectively [36]. When the Rayleigh distance is larger than the distance between the scatterers and the transceiver or between the Tx and Rx, the far-field assumption is not satisfied. In this case, each scatterer and antenna element is abstracted as a point source [31]. The electromagnetic wave propagation model changes from far-field to near-field, which can further be divided into wideband near-field model and narrowband near-field model. If the delay difference in MPC reaching different antenna elements cannot be identified, i.e., $D/\lambda \ll f_c/B$, the narrowband near-field model can be applied. Here, f_c and B represent the carrier frequency and signal bandwidth, respectively. Otherwise, a wideband near-field model should be used. The MPCs' parameters are modeled as antenna- and

frequency-dependent to implement wideband near-field model, and the transfer function of the lth MPC at the kth frequency point can be written as

$$
\begin{aligned}
H_{m,n,l}(f_k) = \sum_{P_{\mathrm{Rx}}=1}^{2} \sum_{P_{\mathrm{Tx}}=1}^{2} & \alpha_{l,P_{\mathrm{Rx}},P_{\mathrm{Tx}}} F_{\mathrm{Rx},m,P_{\mathrm{Rx}}}(f_k, \boldsymbol{\Omega}_{\mathrm{Rx},m,l}) \\
& \cdot F_{\mathrm{Tx},n,P_{\mathrm{Tx}}}(f_k, \boldsymbol{\Omega}_{\mathrm{Tx},n,l}) e^{-j2\pi f_k \tau_{m,n,l}}.
\end{aligned} \tag{3}
$$

Here, $\boldsymbol{\Omega}_{\mathrm{Rx},m,l}$ represents the unit direction vector of the lth MPC of the mth antenna at the Rx side, and $\boldsymbol{\Omega}_{\mathrm{Tx},n,l}$ denotes the unit direction vector of the lth MPC of the nth antenna at the Tx side. Note that the antenna complex gain is modeled as frequency-dependent under wideband condition. Besides, $F_{\mathrm{Rx},m,P_{\mathrm{Rx}}}(f_k, \boldsymbol{\Omega}_{\mathrm{Rx},m,l})$ denotes the complex gain of P_{Rx}-polarization of the mth Rx antenna at the kth frequency point in direction $\boldsymbol{\Omega}_{\mathrm{Rx},m,l}$, and $F_{\mathrm{Tx},n,P_{\mathrm{Tx}}}(f_k, \boldsymbol{\Omega}_{\mathrm{Tx},n,l})$ denotes the same thing at the Tx side. In addition, $\tau_{m,n,l}$ represents the delay of the lth MPC between the mth Rx antenna and the nth Tx antenna. This can be calculated by

$$
\tau_{m,n,l} = \tau_l + \tau_{\mathrm{Rx},m,l} + \tau_{\mathrm{Tx},n,l} \tag{4}
$$

where $\tau_{\mathrm{Rx},m,l} = ((d_{\mathrm{Rx},m,l} - d_{\mathrm{Rx},l})/c)$ represents the delay difference between the mth antenna and reference antenna at the Rx side of the lth MPC, and $\tau_{\mathrm{Tx},n,l} = ((d_{\mathrm{Tx},n,l} - d_{\mathrm{Tx},l}/c)$ denotes the delay difference between the nth antenna and the reference antenna at the Tx side of the lth MPC. Besides, $d_{\mathrm{Rx},m,l}$ and $d_{\mathrm{Rx},l}$ denote the distance of the lth last-bounce scatterer to the mth antenna and the reference antenna at the Rx side, respectively. Meanwhile, $d_{\mathrm{Tx},n,l}$ and $d_{\mathrm{Tx},l}$ represent the distance of the lth first-bounce scatterer to the nth antenna and the reference antenna at the Tx side, respectively. The light speed is denoted by c. Moreover, $d_{\mathrm{Rx},m,l}, d_{\mathrm{Tx},m,l}, \boldsymbol{\Omega}_{\mathrm{Rx},m,l}$, and $\boldsymbol{\Omega}_{\mathrm{Tx},n,l}$ can be calculated by [31]

$$
d_{\mathrm{Rx},m,l} = \left\| d_{\mathrm{Rx},l} \boldsymbol{\Omega}_{\mathrm{Rx},l} - \boldsymbol{r}_{\mathrm{Rx},m} \right\| \tag{5}
$$

$$
d_{\mathrm{Tx},n,l} = \left\| d_{\mathrm{Tx},l} \boldsymbol{\Omega}_{\mathrm{Tx},l} - \boldsymbol{r}_{\mathrm{Tx},n} \right\| \tag{6}
$$

$$
\boldsymbol{\Omega}_{\mathrm{Rx},m,l} = \frac{d_{\mathrm{Rx},l} \boldsymbol{\Omega}_{\mathrm{Rx},l} - \boldsymbol{r}_{\mathrm{Rx},m}}{d_{\mathrm{Rx},m,l}} \tag{7}
$$

$$
\boldsymbol{\Omega}_{\mathrm{Tx},n,l} = \frac{d_{\mathrm{Tx},l} \boldsymbol{\Omega}_{\mathrm{Tx},l} - \boldsymbol{r}_{\mathrm{Tx},m}}{d_{\mathrm{Tx},n,l}} \tag{8}
$$

where $\|\cdot\|$ represents the Frobenius norm. Therefore, parameters of the lth MPC can be represented by set $\boldsymbol{\Gamma}_l$

$$
\begin{aligned}
\boldsymbol{\Gamma}_l = \big\{ & \Re\{\alpha_{l,1,1}, \alpha_{l,1,2}, \alpha_{l,2,1}, \alpha_{l,2,2}\}, \\
& \Im\{\alpha_{l,1,1}, \alpha_{l,1,2}, \alpha_{l,2,1}, \alpha_{l,2,2}\}, \\
& d_{\mathrm{Tx},l}, d_{\mathrm{Rx},l}, \tau_l, \theta_{\mathrm{Tx},l}, \theta_{\mathrm{Rx},l}, \phi_{\mathrm{Tx},l}, \phi_{\mathrm{Rx},l} \big\} \in \mathbb{R}^{15}
\end{aligned} \tag{9}
$$

where $\Re\{\cdot\}$ and $\Im\{\cdot\}$ represent the real and imaginary parts, respectively. For convenience, the transfer function of the lth MPC is given by $\mathbf{H}(\boldsymbol{f}; \boldsymbol{\Gamma}_l) \in \mathbb{C}^{M \times N \times K}$ and the arrangement of this matrix is [31]

$$
\begin{aligned}
\mathbf{H}(\boldsymbol{f}; \boldsymbol{\Gamma}_l) &= \left[\mathbf{H}_{m,n}(\boldsymbol{f}; \boldsymbol{\Gamma}_l) \right]_{M \times N \times K} \\
&= \begin{bmatrix} \mathbf{H}_{1,1}(\boldsymbol{f}; \boldsymbol{\Gamma}_l) & \cdots & \mathbf{H}_{1,N}(\boldsymbol{f}; \boldsymbol{\Gamma}_l) \\ \vdots & \vdots & \vdots \\ \mathbf{H}_{M,1}(\boldsymbol{f}; \boldsymbol{\Gamma}_l) & \cdots & \mathbf{H}_{M,N}(\boldsymbol{f}; \boldsymbol{\Gamma}_l) \end{bmatrix}
\end{aligned} \tag{10}
$$

where $\mathbf{H}_{m,n}(\boldsymbol{f};\boldsymbol{\Gamma}_l) \in \mathbb{C}^{K\times 1}$ represents the transfer function of the lth MPC between the mth Rx antenna and the nth Tx antenna. The kth component of $\mathbf{H}_{m,n}(\boldsymbol{f};\boldsymbol{\Gamma}_l)$ can be calculated by (3).

The transfer function of the lth MPC at the kth frequency point can be written in matrix form as

$$\mathbf{H}(f_k;\boldsymbol{\Gamma}_l) = \mathbf{F}_{\mathrm{Rx}}(f_k,\boldsymbol{\Omega}_{\mathrm{Rx},l},d_{\mathrm{Rx},l})\mathbf{A}_l\mathbf{F}_{\mathrm{Tx}}(f_k,\boldsymbol{\Omega}_{\mathrm{Tx},l},d_{\mathrm{Tx},l})^T \\ \odot e^{-j2\pi f_k\boldsymbol{\Psi}_l}. \quad (11)$$

It should be noted that the channel matrix $\mathbf{H}(f_k;\boldsymbol{\Gamma}_l) \in \mathbb{C}^{M\times N}$ is the kth $M \times N$ array slice defined by the third dimension of $\mathbf{H}(\boldsymbol{f};\boldsymbol{\Gamma}_l)$. Here, the symbol $\odot$ represents the elementwise product, $\mathbf{A}_l = [\alpha_{l,P_{\mathrm{Rx}},P_{\mathrm{Tx}}};\ P_{\mathrm{Rx/Tx}} = 1,2] \in \mathbb{C}^{2\times 2}$ represents the complex gain of the lth MPC, and $\boldsymbol{\Psi}_l = [\tau_{m,n,l};\ m = 1,\dots,M,\ n = 1,\dots,N] \in \mathbb{R}^{M\times N}$ represents the delay matrix of the lth MPC over the antenna array. In addition, $\mathbf{F}_{\mathrm{Rx}}(f_k,\boldsymbol{\Omega}_{\mathrm{Rx},l},d_{\mathrm{Rx},l}) \in \mathbb{C}^{M\times 2}$ denotes the complex gain of Rx antenna array of the lth MPC at the kth frequency, and it can be expressed by [31]

$$\begin{aligned} &\mathbf{F}_{\mathrm{Rx}}(f_k,\boldsymbol{\Omega}_{\mathrm{Rx},l},d_{\mathrm{Rx},l}) \\ &= \left[F_{\mathrm{Rx},m,P_{\mathrm{Rx}}}(f_k,\boldsymbol{\Omega}_{\mathrm{Rx},m,l})\right]_{M\times 2} \\ &= \begin{bmatrix} F_{\mathrm{Rx},1,1}(f_k,\boldsymbol{\Omega}_{\mathrm{Rx},1,l}) & F_{\mathrm{Rx},1,2}(f_k,\boldsymbol{\Omega}_{\mathrm{Rx},1,l}) \\ \vdots & \vdots \\ F_{\mathrm{Rx},m,1}(f_k,\boldsymbol{\Omega}_{\mathrm{Rx},m,l}) & F_{\mathrm{Rx},m,2}(f_k,\boldsymbol{\Omega}_{\mathrm{Rx},m,l}) \end{bmatrix}. \end{aligned} \quad (12)$$

Meanwhile, $\mathbf{F}_{\mathrm{Tx}}(f_k,\boldsymbol{\Omega}_{\mathrm{Tx},l},d_{\mathrm{Tx},l}) \in \mathbb{C}^{N\times 2}$ represents the complex gain of the Tx antenna array of the lth MPC at the kth frequency point, and it can be denoted by [31]

$$\begin{aligned} &\mathbf{F}_{\mathrm{Tx}}(f_k,\boldsymbol{\Omega}_{\mathrm{Tx},l},d_{\mathrm{Tx},l}) \\ &= \left[F_{\mathrm{Tx},n,P_{\mathrm{Tx}}}(f_k,\boldsymbol{\Omega}_{\mathrm{Tx},n,l})\right]_{N\times 2} \\ &= \begin{bmatrix} F_{\mathrm{Tx},1,1}(f_k,\boldsymbol{\Omega}_{\mathrm{Tx},1,l}) & F_{\mathrm{Tx},1,2}(f_k,\boldsymbol{\Omega}_{\mathrm{Tx},1,l}) \\ \vdots & \vdots \\ F_{\mathrm{Tx},n,1}(f_k,\boldsymbol{\Omega}_{\mathrm{Tx},n,l}) & F_{\mathrm{Tx},n,2}(f_k,\boldsymbol{\Omega}_{\mathrm{Tx},n,l}) \end{bmatrix}. \end{aligned} \quad (13)$$

C. Wideband Spatial Nonstationary Signal Model With Antenna Polarization

It is assumed that the MPCs can reach all the antennas uniformly at the wideband near-field signal model as expressed in (11). However, as the aperture of the antenna array increases, this assumption may not hold. In the mmWave massive MIMO scenarios, the birth–death of MPCs in the antenna array axis can be observed [19], [37], where some MPCs become invisible to part of the antennas due to near-field blocking effects, as shown in Fig. 1. To describe the channel more accurately, the birth–death coefficients $\boldsymbol{\zeta}_{\mathrm{Rx}}$ and $\boldsymbol{\zeta}_{\mathrm{Tx}}$ are introduced in the wideband near-field model to characterize the birth–death of the MPCs at the Rx side and Tx side, respectively. The proposed spatial nonstationary signal model of the lth MPC at the kth frequency point is denoted by $\mathbf{H}(f_k;\boldsymbol{\Theta}_l) \in \mathbb{C}^{M\times N}$, which can be expressed by

$$\mathbf{H}(f_k;\boldsymbol{\Theta}_l) = \mathbf{H}(f_k;\boldsymbol{\Gamma}_l) \odot \left(\boldsymbol{\zeta}_{\mathrm{Rx},l}\boldsymbol{\zeta}_{\mathrm{Tx},l}^T\right) \quad (14)$$

where $\boldsymbol{\Theta}_l = \{\boldsymbol{\zeta}_{\mathrm{Rx},l},\boldsymbol{\zeta}_{\mathrm{Tx},l},\boldsymbol{\Gamma}_l\}$ denotes the parameters' set of the lth MPC in the spatial nonstationary signal model,

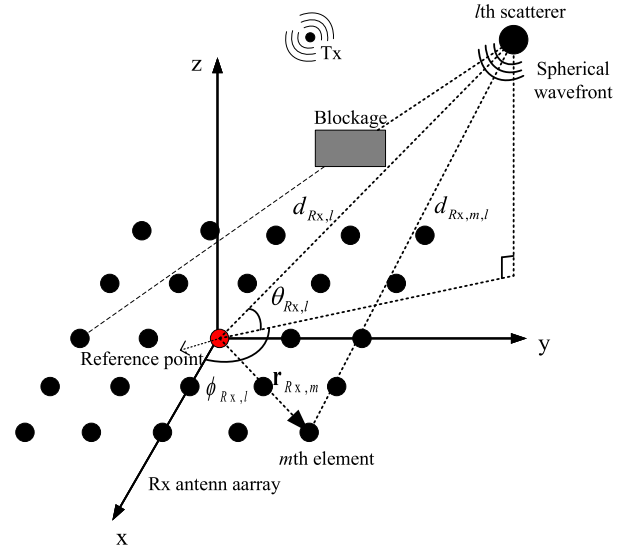Fig. 1. Near-field propagation channel with spatial nonstationarity at the Rx side.

and $\boldsymbol{\zeta}_{\mathrm{Rx},l} = [\zeta_{\mathrm{Rx},1,l},\dots,\zeta_{\mathrm{Rx},M,l}]^T \in \mathbb{R}^{M\times 1}$ represents the birth–death coefficient of the lth MPC at the Rx side. The value of $\zeta_{\mathrm{Rx},m,l}$ is 0 or 1, where $\zeta_{\mathrm{Rx},m,l} = 1$ indicates that the lth MPC is visible to the mth antenna at Rx. Besides, $\boldsymbol{\zeta}_{\mathrm{Tx},l} = [\zeta_{\mathrm{Tx},1,l},\dots,\zeta_{\mathrm{Tx},N,l}]^T \in \mathbb{R}^{N\times 1}$ denotes the birth–death coefficient of the lth MPC at the Tx side. If all the elements in $\boldsymbol{\zeta}_{\mathrm{Rx},l}$ and $\boldsymbol{\zeta}_{\mathrm{Tx},l}$ equal to 1, the channel model in (14) is the same as the wideband near-field model in (11). Otherwise, $\zeta_{\mathrm{Rx},m,l} = 0$ means that this MPC is invisible to the mth antenna at Rx.

The measured channel transfer function (CTF) $\mathbf{Y}(\boldsymbol{f}) \in \mathbb{C}^{M\times N\times K}$ can be expressed as [35]

$$\mathbf{Y}(\boldsymbol{f}) = \sum_{l=1}^{L}\mathbf{H}(\boldsymbol{f},\boldsymbol{\Theta}_l) + \sqrt{\frac{\sigma_n^2}{2}}\boldsymbol{n}(\boldsymbol{f}) \quad (15)$$

where $\boldsymbol{n}(\boldsymbol{f}) \in \mathbb{C}^{M\times N\times K}$ denotes the noise matrix, in which each element is assumed to follow an independent and identical standard complex Gaussian distribution with zero mean and unit variance. In addition, σ_n^2 represents the variance of noise matrix, and L denotes the total number of MPCs. To simplify the notation, we further define [15]

$$\mathbf{H}(\boldsymbol{f};\boldsymbol{\Theta}) = \sum_{l=1}^{L}\mathbf{H}(\boldsymbol{f},\boldsymbol{\Theta}_l) \quad (16)$$

where $\boldsymbol{\Theta} = \{\boldsymbol{\Theta}_1,\dots,\boldsymbol{\Theta}_L\}$ denotes the set of parameters of all the MPCs. The key parameters of the above three signal models are listed in Table I.

III. PROPOSED SAGE-WSNSAP ALGORITHM

The ML-based estimators can be derived from measurements to solve the CPE problem defined in (15). In this section, the ML-based estimators will be introduced first, and then we give the detailed implementation process of the proposed algorithm.

TABLE I
DEFINITION OF KEY PARAMETERS FOR THREE SIGNAL MODELS

$\alpha_{l,P_{\text{Rx}},P_{\text{Tx}}}$	The complex attenuation of the lth MPC undergoing P_{Rx}-polarization and P_{Tx}-polarization
$\mathbf{\Omega}_{\text{Rx},l}$, $\mathbf{\Omega}_{\text{Tx},l}$	The AoD and AoA of the lth MPC
$\mathbf{F}_{\text{Tx},n,P_{\text{Tx}}}(\mathbf{\Omega}_{\text{Tx},l})$	The complex gain of P_{Tx}-polarization of the nth Tx antenna in the direction $\mathbf{\Omega}_{\text{Tx},l}$
$\mathbf{F}_{\text{Rx},n,P_{\text{Rx}}}(\mathbf{\Omega}_{\text{Rx},l})$	The complex gain of P_{Rx}-polarization of the mth Rx antenna in the direction $\mathbf{\Omega}_{\text{Rx},l}$
$\mathbf{\Omega}_{\text{Rx},m,l}$	The unit direction vector of the lth MPC of the mth antenna at the Rx side
$\mathbf{\Omega}_{\text{Tx},n,l}$	The unit direction vector of the lth MPC of the nth antenna at the Tx side
$\mathbf{F}_{\text{Rx},m,P_{\text{Rx}}}(f_k,\mathbf{\Omega}_{\text{Rx},m,l})$	The complex gain of P_{Rx}-polarization of the mth Rx antenna at the kth frequency point in the direction $\mathbf{\Omega}_{\text{Rx},m,l}$
$\mathbf{F}_{\text{Tx},n,P_{\text{Tx}}}(f_k,\mathbf{\Omega}_{\text{Tx},n,l})$	The complex gain of P_{Tx}-polarization of the nth Tx antenna at the kth frequency point in the direction $\mathbf{\Omega}_{\text{Tx},n,l}$
τ_l	The delay of the lth MPC
$\tau_{m,n,l}$	The delay of the lth MPC between the mth Rx antenna and the nth Tx antenna
$\boldsymbol{f}$	The measurement frequency vector
$d_{\text{Rx},m,l}, d_{\text{Rx},l}$	The distance of the lth last-bounce scatterer to the mth antenna and the reference antenna at the Rx side
$d_{\text{Tx},n,l}, d_{\text{Tx},l}$	The distance of the lth first-bounce scatterer to the nth antenna and the reference antenna at the Tx side
$\boldsymbol{r}_{\text{Rx},m}, \boldsymbol{r}_{\text{Tx},n}$	The position vectors of the mth Rx antenna and nth Tx antenna
$\boldsymbol{\Gamma}_l$	The parameter set that constitutes the lth MPC in wideband near-field model
$\mathbf{A}_l$	The complex gain of the lth MPC
$\boldsymbol{\Psi}_l$	The delay matrix of the lth MPC
$\boldsymbol{\zeta}_{\text{Rx},l}, \boldsymbol{\zeta}_{\text{Tx},l}$	The birth-death coefficients of the lth MPC at the Rx side and the Tx side
$\boldsymbol{\Theta}_l$	The parameter set that constitutes the lth MPC in spatial non-stationary channel model
$\boldsymbol{\Theta}$	The set of parameters of all MPCs
$\mathbf{Y}(\boldsymbol{f})$	The measured CTF
$\boldsymbol{n}(\boldsymbol{f})$	The measured noise matrix
L	Total number of MPCs

A. ML-Based Estimator

The expectation of the log-likelihood function can be calculated by [13]

$$\mathbf{E}[\Lambda(\boldsymbol{\Theta}; \mathbf{Y}(\boldsymbol{f}))] = -2\ln(\pi\sigma_n^2) - \frac{1}{\sigma_n^2 MNK}$$
$$\cdot \|\text{vec}\{\mathbf{Y}(\boldsymbol{f})\} - \text{vec}\{\mathbf{H}(\boldsymbol{f};\boldsymbol{\Theta})\}\|^2 \quad (17)$$

where $\mathbf{E}[\cdot]$ represents the expectation operation, and $\text{vec}\{\cdot\}$ denotes the vectorization operation. The estimation of parameters' set $\boldsymbol{\Theta}$ is obtained by maximizing the likelihood function in (17), and it can be given by

$$\hat{\boldsymbol{\Theta}} = \underset{\boldsymbol{\Theta}}{\arg\max}\left\{\mathbf{E}[\Lambda(\boldsymbol{\Theta};\mathbf{Y}(\boldsymbol{f}))]\right\}. \quad (18)$$

In practice, the dimension of $\boldsymbol{\Theta}$ is so large that brute-force retrieval of (18) is not feasible. To solve this problem, the successive interference cancellation (SIC) method was proposed in [38] and [39], where the MPCs are assumed orthogonal to each other. In SIC, the MPCs are extracted in order of power and can effectively reduce the interference of strong MPCs to weak MPCs. Moreover, the delay and angle resolution of MPCs in wideband massive MIMO systems are relatively high. If the delay or angle difference of two MPCs is larger than the resolution of the corresponding domain, the two MPCs can be considered to be orthogonal to each other [30]. Therefore, the SIC method can be used in this article to sequentially extract the parameters of each MPC. The estimation of the lth MPC in SIC is to find the maximum value of [35]

$$\hat{\boldsymbol{\Theta}}_l = \underset{\boldsymbol{\Theta}_l}{\arg\max}\left\{\mathbf{E}[\Lambda(\boldsymbol{\Theta}_l;\mathbf{Y}_l(\boldsymbol{f}))]\right\} \quad (19)$$

where $\mathbf{Y}_l(\boldsymbol{f}) \in \mathbb{C}^{N\times M\times K}$ represents the expectation of the lth MPC from the measured CTF and can be calculated by [15]

$$\mathbf{Y}_l(\boldsymbol{f}) = \begin{cases} \mathbf{Y}(\boldsymbol{f}), & \text{if } l = 1. \\ \mathbf{Y}(\boldsymbol{f}) - \sum_{l'=1}^{l-1}\mathbf{H}(\boldsymbol{f};\hat{\boldsymbol{\Theta}}_{l'}), & \text{if } l \in [2,\dots,L]. \end{cases} \quad (20)$$

The first MPC is estimated from the measurement data $\mathbf{Y}(\boldsymbol{f})$. Then, the reconstructed transfer function given by (14) is subtracted from the measurement data, and the residual part is used to estimate the next MPC. Repeat this procedure until L MPCs are estimated. In addition, it can be proved that maximizing the log-likelihood function in (19) is equivalent to maximizing the object function $z(\boldsymbol{f};\boldsymbol{\Theta}_l^\alpha)$ as [40]

$$\hat{\boldsymbol{\Theta}}_l^\alpha = \underset{\boldsymbol{\Theta}_l^\alpha}{\arg\max}\left\{z(\boldsymbol{f};\boldsymbol{\Theta}_l^\alpha)\right\} \quad (21)$$

where $\boldsymbol{\Theta}_l^\alpha = \{\boldsymbol{\zeta}_{\text{Rx},l}, \boldsymbol{\zeta}_{\text{Tx},l}, \boldsymbol{\Omega}_{\text{Rx},l}, \boldsymbol{\Omega}_{\text{Tx},l}, d_{\text{Rx},l}, d_{\text{Tx},l}, \tau_l\}$ represents the parameter set of the lth MPC without $\boldsymbol{\alpha}_l$, and $z(\boldsymbol{f};\boldsymbol{\Theta}_l^\alpha)$ can be calculated by

$$z(\boldsymbol{f};\boldsymbol{\Theta}_l^\alpha) = \left\|\sum_{k=1}^K \boldsymbol{g}(f_k;\boldsymbol{\Theta}_l^\alpha)^H \mathbf{G}(\mathbf{C}_{\text{Rx},k,l},\mathbf{C}_{\text{Tx},k,l})^{-1}\boldsymbol{g}(f_k;\boldsymbol{\Theta}_l^\alpha)\right\| \quad (22)$$

where $[\cdot]^H$ denotes the conjugate transpose operation, and

$$\boldsymbol{g}(f_k;\boldsymbol{\Theta}_l^\alpha) = \begin{bmatrix} \boldsymbol{c}_{\text{Rx},1,k,l}^H \mathbf{X}_l(f_k,\tau_l)\boldsymbol{c}_{\text{Tx},1,k,l}^* \\ \boldsymbol{c}_{\text{Rx},1,k,l}^H \mathbf{X}_l(f_k,\tau_l)\boldsymbol{c}_{\text{Tx},2,k,l}^* \\ \boldsymbol{c}_{\text{Rx},2,k,l}^H \mathbf{X}_l(f_k,\tau_l)\boldsymbol{c}_{\text{Tx},1,k,l}^* \\ \boldsymbol{c}_{\text{Rx},2,k,l}^H \mathbf{X}_l(f_k,\tau_l)\boldsymbol{c}_{\text{Tx},2,k,l}^* \end{bmatrix}. \quad (23)$$

Here, $[\cdot]^*$ denotes the conjugate operation. Besides, $\mathbf{X}_l(f_k,\tau_l) \in \mathbb{C}^{M\times N}$ can be calculated by

$$\mathbf{X}_l(f_k,\tau_l) = \mathbf{Y}_l(f_k)e^{j2\pi f_k\tau_l} \quad (24)$$

where $\mathbf{Y}_l(f_k) \in \mathbb{C}^{M \times N}$ represents the transfer function of the lth MPC at the kth frequency point. Moreover, $\mathbf{C}_{\mathrm{Rx},k,l} \in \mathbb{C}^{M \times 2}$ and $\mathbf{C}_{\mathrm{Tx},k,l} \in \mathbb{C}^{N \times 2}$ represent the steering vector of the lth MPC at the kth frequency point at the Rx side and the Tx side, respectively. Taking the calculation of steering vector at the Rx side as an example, the steering vector at the Tx side can be calculated in the same way. The steering vector at the Rx side can be expressed as

$$
\begin{aligned}
\mathbf{C}_{\mathrm{Rx},k,l} &= \left[\boldsymbol{c}_{\mathrm{Rx}, P_{\mathrm{Rx}}, k, l} \right]_{N \times 2} \\
&= \left[\mathbf{F}_{\mathrm{Rx},1}(f_k, \boldsymbol{\Omega}_{\mathrm{Rx},l}, d_{\mathrm{Rx},l}) \odot \boldsymbol{\zeta}_{\mathrm{Rx},l} \odot \boldsymbol{\varepsilon}_{\mathrm{Rx},k,l}, \right. \\
&\quad \left. \mathbf{F}_{\mathrm{Rx},2}(f_k, \boldsymbol{\Omega}_{\mathrm{Rx},l}, d_{\mathrm{Rx},l}) \odot \boldsymbol{\zeta}_{\mathrm{Rx},l} \odot \boldsymbol{\varepsilon}_{\mathrm{Rx},k,l} \right]
\end{aligned} \quad (25)
$$

where $\boldsymbol{\varepsilon}_{\mathrm{Rx},k,l} = e^{-j2\pi f_k \boldsymbol{\tau}_{\mathrm{Rx},l}}$ represents the phase difference of the lth MPC at the Rx side at the kth frequency point. Here, $\boldsymbol{\tau}_{\mathrm{Rx},l} = [\tau_{\mathrm{Rx},1,l}, \ldots, \tau_{\mathrm{Rx},M,l}]^T \in \mathbb{R}^{M \times 1}$ is the delay difference between the lth last-bounce scatterer to the reference antenna and that to other elements at the Rx side. The matrix $\mathbf{G} \in \mathbb{C}^{4 \times 4}$ in (22) can be calculated by [38]

$$
\mathbf{G}(\mathbf{C}_{\mathrm{Rx},k,l}, \mathbf{C}_{\mathrm{Tx},k,l}) = \left[\mathbf{C}_{\mathrm{Rx},k,l}^H \mathbf{C}_{\mathrm{Rx},k,l} \right] \otimes \left[\mathbf{C}_{\mathrm{Tx},k,l}^H \mathbf{C}_{\mathrm{Tx},k,l} \right] \quad (26)
$$

where $\otimes$ denotes the Kronecker product, and the estimation result of $\hat{\boldsymbol{\alpha}}_l$ is obtained by

$$
\hat{\boldsymbol{\alpha}}_l = \frac{1}{K} \sum_{k=1}^{K} \mathbf{G}(\mathbf{C}_{\mathrm{Rx},k,l}, \mathbf{C}_{\mathrm{Tx},k,l})^{-1} \boldsymbol{g}(f_k; \boldsymbol{\Theta}_l^{\alpha}). \quad (27)
$$

B. Procedure of the Proposed SAGE-WSNSAP Algorithm

To reduce the computational complexity, a coarse-to-fine search strategy is adopted in the initialization process. The coarse search step is to estimate the delays and angles of the MPCs based on the narrowband far-field assumption. Therefore, part of frequency points near the center frequency from the wideband measurement data is extracted, resulting in narrowband signal $\mathbf{Y}(f_{\mathrm{narr}})$. In this case, the parameter space of delay and angle is guaranteed to satisfy orthogonal stochastic measures (OSMs) [13], making the traditional SAGE method feasible. With the prior knowledge of coarse estimation, the search space can be limited in the refinement step, which is under the near-field assumption. The coarse-to-fine search process ignores the birth and death of MPCs in the spatial domain, indicating that $\boldsymbol{\zeta}_{\mathrm{Rx},l}$ and $\boldsymbol{\zeta}_{\mathrm{Tx},l}$ are both set to 1. In the next step, these two parameters are estimated based on the ML principle. Finally, the cancellation and retention of MPCs are determined.

1) Parameter Coarse Search Under the Narrowband Far-Field Assumption: The initial delay, AoA, and AoD of the lth MPC will be estimated at this step. The initial estimation of delay $\hat{\tau}_l^{\mathrm{init}}$ is obtained by

$$
\hat{\tau}_l^{\mathrm{init}} = \arg\max_{\tau_l} \left\{ \sum_{m=1}^{M} \sum_{n=1}^{N} \left\| \mathbf{Y}_{m,n,l}(f_{\mathrm{narr}}) e^{j2\pi f_{\mathrm{narr}} \tau_l} \right\|^2 \right\}. \quad (28)
$$

Note that the search range for τ_l is $[0, (1/B_{\mathrm{narr}}), \ldots, (M_{\mathrm{narr}}/B_{\mathrm{narr}})]^T$, where B_{narr} represents the bandwidth of narrowband signal $\mathbf{Y}(f_{\mathrm{narr}}) \in \mathbb{C}^{M \times N \times M_{\mathrm{narr}}}$,

and M_{narr} denotes the number of frequency points of f_{narr}. Then the initial estimation of AoA $\hat{\boldsymbol{\Omega}}_{\mathrm{Rx},l}^{\mathrm{init}}$ is calculated by

$$
\begin{aligned}
\hat{\boldsymbol{\Omega}}_{\mathrm{Rx},l}^{\mathrm{init}} = \arg\max_{\boldsymbol{\Omega}_{\mathrm{Rx},l}} &\sum_{n=1}^{N} \left\| \left[\mathbf{C}_{\mathrm{Rx},l,\mathrm{init}}^H \mathbf{X}_{:,n,l}(f_{\mathrm{narr}}, \hat{\tau}_l^{\mathrm{init}}) \right]^H \right. \\
&\times \left. \left[\mathbf{C}_{\mathrm{Rx},l,\mathrm{init}}^H \mathbf{C}_{\mathrm{Rx},l,\mathrm{init}} \right]^{-1} \left[\mathbf{C}_{\mathrm{Rx},l,\mathrm{init}}^H \mathbf{X}_{:,n,l}(f_{\mathrm{narr}}, \hat{\tau}_l^{\mathrm{init}}) \right] \right\|
\end{aligned} \quad (29)
$$

where $\mathbf{C}_{\mathrm{Rx},l,\mathrm{init}} \in \mathbb{C}^{M \times 2}$ represents the array steering vector of Rx used in the coarse search step and is calculated based on the far-field assumption. The mth element of $\mathbf{C}_{\mathrm{Rx},l,\mathrm{init}}$ is calculated by

$$
\mathbf{C}_{\mathrm{Rx},m,l,\mathrm{init}} = \left[F_{\mathrm{Rx},m,1}(\boldsymbol{\Omega}_{\mathrm{Rx},l}) e^{j\frac{2\pi}{\lambda} \langle \boldsymbol{\Omega}_{\mathrm{Rx},l} \cdot \boldsymbol{r}_{\mathrm{Rx},m} \rangle}, \right.
$$
$$
\left. F_{\mathrm{Rx},m,2}(\boldsymbol{\Omega}_{\mathrm{Rx},l}) e^{j\frac{2\pi}{\lambda} \langle \boldsymbol{\Omega}_{\mathrm{Rx},l} \cdot \boldsymbol{r}_{\mathrm{Rx},m} \rangle} \right]. \quad (30)
$$

Here, $\mathbf{X}_{:,n,l}(f_{\mathrm{narr}}, \hat{\tau}_l^{\mathrm{init}})$ represents the nth column of the matrix $\mathbf{X}_l(f_{\mathrm{narr}}, \hat{\tau}_l^{\mathrm{init}})$ with size of $M \times N$, and the (m,n)th component of that is calculated by

$$
\mathbf{X}_{m,n,l}(f_{\mathrm{narr}}, \hat{\tau}_l^{\mathrm{init}}) = \mathbf{Y}_{m,n,l}(f_{\mathrm{narr}}) e^{j2\pi f_{\mathrm{narr}} \hat{\tau}_l^{\mathrm{init}}}. \quad (31)
$$

The initial estimation of AoD $\hat{\boldsymbol{\Omega}}_{\mathrm{Tx},l}^{\mathrm{init}}$ is obtained by

$$
\hat{\boldsymbol{\Omega}}_{\mathrm{Tx},l}^{\mathrm{init}} = \arg\max_{\boldsymbol{\Omega}_{\mathrm{Tx},l}} \boldsymbol{g}(f_{\mathrm{narr}}; \boldsymbol{\Theta}_l^{\alpha})^H \mathbf{G}(\hat{\mathbf{C}}_{\mathrm{Rx},l,\mathrm{init}}, \mathbf{C}_{\mathrm{Tx},l,\mathrm{init}})^{-1}
$$
$$
\times \boldsymbol{g}(f_{\mathrm{narr}}; \boldsymbol{\Theta}_l^{\alpha}) \quad (32)
$$

where $\hat{\mathbf{C}}_{\mathrm{Rx},l,\mathrm{init}}$ represents the estimated steering vector of Rx, and it can be calculated based on (30) with $\boldsymbol{\Omega}_{\mathrm{Rx},l} = \hat{\boldsymbol{\Omega}}_{\mathrm{Rx},l}^{\mathrm{init}}$. $\mathbf{C}_{\mathrm{Tx},l,\mathrm{init}} \in \mathbb{C}^{N \times 2}$ is calculated in the same way as $\mathbf{C}_{\mathrm{Rx},l,\mathrm{init}}$ by replacing $\boldsymbol{\Omega}_{\mathrm{Rx},l}$ and $\boldsymbol{r}_{\mathrm{Rx}}$ with $\boldsymbol{\Omega}_{\mathrm{Tx},l}$ and $\boldsymbol{r}_{\mathrm{Tx}}$, respectively. The antenna pattern at center frequency is used when calculating $\mathbf{C}_{\mathrm{Rx},l,\mathrm{init}}$ and $\mathbf{C}_{\mathrm{Tx},l,\mathrm{init}}$. Besides, note that when calculating $\boldsymbol{g}(f_k; \boldsymbol{\Theta}_l^{\alpha})$ in (23), it needs to replace $\mathbf{C}_{\mathrm{Rx},k,l}$ and $\mathbf{C}_{\mathrm{Tx},k,l}$ with $\mathbf{C}_{\mathrm{Rx},l,\mathrm{init}}$ and $\mathbf{C}_{\mathrm{Tx},l,\mathrm{init}}$, respectively. So far, the initial estimation of the lth MPC is $(\hat{\boldsymbol{\Theta}}_l^{\alpha})^{\mathrm{init}} = \{\hat{\boldsymbol{\Omega}}_{\mathrm{Rx},l}^{\mathrm{init}}, \hat{\boldsymbol{\Omega}}_{\mathrm{Tx},l}^{\mathrm{init}}, \hat{\tau}_l^{\mathrm{init}}\}$.

2) Parameter Refinement Under the Near-Field Assumption: The refined search will be conducted at this step under the spherical wave assumption to improve the estimation accuracy of $\hat{\boldsymbol{\Theta}}_l^{\alpha}$. The $\boldsymbol{\Omega}_{\mathrm{Rx},l}$ and $d_{\mathrm{Rx},l}$ can be estimated by solving the following 3-D search problem:

$$
\begin{aligned}
\{\hat{\boldsymbol{\Omega}}_{\mathrm{Rx},l}, \hat{d}_{\mathrm{Rx},l}\} = \arg\max_{\boldsymbol{\Omega}_{\mathrm{Rx},l}, d_{\mathrm{Rx},l}} &\sum_{n=1}^{N} \left\| \left[\mathbf{C}_{\mathrm{Rx},l}^H \mathbf{X}_{:,n,l}(f_{\mathrm{narr}}, \hat{\tau}_l^{\mathrm{init}}) \right]^H \right. \\
&\times \left. \left[\mathbf{C}_{\mathrm{Rx},l}^H \mathbf{C}_{\mathrm{Rx},l} \right]^{-1} \left[\mathbf{C}_{\mathrm{Rx},l}^H \mathbf{X}_{:,n,l}(f_{\mathrm{narr}}, \hat{\tau}_l^{\mathrm{init}}) \right] \right\|
\end{aligned} \quad (33)
$$

where $\mathbf{C}_{\mathrm{Rx},l} \in \mathbb{C}^{M \times 2}$ is calculated based on (25) at center frequency. The prior knowledge of $\hat{\boldsymbol{\Omega}}_{\mathrm{Rx},l}^{\mathrm{init}}$ can significantly reduce the search space of this maximization problem. Then, the estimation results of $\boldsymbol{\Omega}_{\mathrm{Tx},l}$ and $d_{\mathrm{Tx},l}$ are obtained by

$$
\begin{aligned}
&\{\hat{\boldsymbol{\Omega}}_{\mathrm{Tx},l}, \hat{d}_{\mathrm{Tx},l}\} \\
&= \arg\max_{\boldsymbol{\Omega}_{\mathrm{Tx},l}, d_{\mathrm{Tx},l}} \boldsymbol{g}(f_{\mathrm{narr}}; \hat{\boldsymbol{\Theta}}_l^{\alpha})^H \mathbf{G}(\hat{\mathbf{C}}_{\mathrm{Rx},l}, \mathbf{C}_{\mathrm{Tx},l})^{-1} \boldsymbol{g}(f_{\mathrm{narr}}; \hat{\boldsymbol{\Theta}}_l^{\alpha}).
\end{aligned} \quad (34)
$$

Here, $\hat{\boldsymbol{\Theta}}_l^{\alpha} = \{\hat{\boldsymbol{\Omega}}_{\mathrm{Rx},l}, \hat{d}_{\mathrm{Rx},l}, \hat{\tau}_l^{\mathrm{init}}\}$, and $\hat{\mathbf{C}}_{\mathrm{Rx},l}$ represents the estimated array steering vector of Rx calculated based on

(25) with $\hat{\boldsymbol{\Omega}}_{\text{Rx},l}$ and $\hat{d}_{\text{Rx},l}$. The Tx array steering vector $\mathbf{C}_{\text{Tx},l} \in \mathbb{C}^{N \times 2}$ used here is also obtained by (25) at the center frequency. Then, the estimation of τ_l is obtained by solving the maximum problem as

$$\hat{\tau}_l = \underset{\tau_l}{\arg\max} \left\| \sum_{k=1}^{K} \boldsymbol{g}(f_k; \hat{\boldsymbol{\Theta}}_l^{\alpha})^H \mathbf{G}(\hat{\mathbf{C}}_{\text{Rx},k,l}, \hat{\mathbf{C}}_{\text{Tx},k,l})^{-1} \boldsymbol{g}(f_k; \hat{\boldsymbol{\Theta}}_l^{\alpha}) \right\|$$
(35)

where $\hat{\boldsymbol{\Theta}}_l^{\alpha} = \{\hat{\boldsymbol{\Omega}}_{\text{Rx},l}, \hat{\boldsymbol{\Omega}}_{\text{Tx},l}, \hat{d}_{\text{Rx},l}, \hat{d}_{\text{Rx},l}\}$. Besides, $\hat{\mathbf{C}}_{\text{Rx},k,l}$ and $\hat{\mathbf{C}}_{\text{Tx},k,l}$ represent the Rx and the Tx estimated array steering vector at the kth frequency point, respectively, which can be calculated based on (25). The estimation of $\hat{\boldsymbol{\alpha}}_l$ is obtained by

$$\hat{\boldsymbol{\alpha}}_l = \frac{1}{K} \sum_{k=1}^{K} \mathbf{G}(\hat{\mathbf{C}}_{\text{Rx},k,l}, \hat{\mathbf{C}}_{\text{Tx},k,l})^{-1} \boldsymbol{g}(f_k; \hat{\boldsymbol{\Theta}}_l^{\alpha})$$
(36)

where $\hat{\boldsymbol{\Theta}}_l^{\alpha} = \{\hat{\boldsymbol{\Omega}}_{\text{Rx},l}, \hat{\boldsymbol{\Omega}}_{\text{Tx},l}, \hat{d}_{\text{Rx},l}, \hat{d}_{\text{Tx},l}, \hat{\tau}_l\}$.

3) MPCs' Birth–Death Identification: The estimation of $\boldsymbol{\zeta}_{\text{Rx},l}$ and $\boldsymbol{\zeta}_{\text{Tx},l}$ will be performed alternately at this step. It can be found that maximizing the likelihood function in (17) is equivalent to minimizing $\|\text{vec}\{\mathbf{Y}_l(\boldsymbol{f})\} - \text{vec}\{\mathbf{H}(\boldsymbol{f}; \boldsymbol{\Theta}_l)\}\|^2$. Therefore, the estimation of the mth component of $\boldsymbol{\zeta}_{\text{Rx},l}$ is obtained by minimizing the following formula:

$$\hat{\zeta}_{\text{Rx},m,l} = \underset{\zeta_{\text{Rx},m,l} \in \{0,1\}}{\arg\min} \left\| \text{vec}\{\mathbf{Y}_{m,:,l}(\boldsymbol{f})\} \right.$$
$$\left. - \text{vec}\{\mathbf{H}_{m,:}(\boldsymbol{f}; \hat{\boldsymbol{\Theta}}_l)\}\zeta_{\text{Rx},m,l} \right\|^2$$
(37)

where $\hat{\boldsymbol{\Theta}}_l = \{\hat{\boldsymbol{\alpha}}_l, \hat{\boldsymbol{\Omega}}_{\text{Rx},l}, \hat{\boldsymbol{\Omega}}_{\text{Tx},l}, \hat{d}_{\text{Rx},l}, \hat{d}_{\text{Tx},l}, \hat{\tau}_l\}$, and $\mathbf{Y}_{m,:,l}(\boldsymbol{f})$ represents the mth $N \times K$ array slice defined by the first dimension of $\mathbf{Y}_l(\boldsymbol{f})$, where $m = 1, \ldots, M$. In addition, $\mathbf{H}_{m,:}(\boldsymbol{f}; \hat{\boldsymbol{\Theta}}_l)$ denotes of the mth $N \times K$ array slice defined by the first dimension of $\mathbf{H}(\boldsymbol{f}; \hat{\boldsymbol{\Theta}}_l)$. Then, the nth element of $\boldsymbol{\zeta}_{\text{Tx},l}$ is estimated following the same principle as

$$\hat{\zeta}_{\text{Tx},n,l} = \underset{\zeta_{\text{Tx},n,l} \in \{0,1\}}{\arg\min} \left\| \text{vec}\{\mathbf{Y}_{:,n,l}(\boldsymbol{f})\} \right.$$
$$\left. - \text{vec}\{\mathbf{H}_{:,n}(\boldsymbol{f}; \hat{\boldsymbol{\Theta}}_l)\}\zeta_{\text{Tx},n,l} \right\|^2$$
(38)

where $\hat{\boldsymbol{\Theta}}_l = \{\hat{\boldsymbol{\zeta}}_{\text{Rx},l}, \hat{\boldsymbol{\alpha}}_l, \hat{\boldsymbol{\Omega}}_{\text{Rx},l}, \hat{\boldsymbol{\Omega}}_{\text{Tx},l}, \hat{d}_{\text{Rx},l}, \hat{d}_{\text{Tx},l}, \hat{\tau}_l\}$, and $\mathbf{Y}_{:,n,l}(\boldsymbol{f})$ represents the nth $M \times K$ array slice defined by the second dimension of $\mathbf{Y}_l(\boldsymbol{f})$, where $n = 1, \ldots, N$. Besides, $\mathbf{H}_{:,n}(\boldsymbol{f}; \hat{\boldsymbol{\Theta}}_l)$ denotes the nth $M \times K$ array slice defined by the second dimension of $\mathbf{H}(\boldsymbol{f}; \hat{\boldsymbol{\Theta}}_l)$. So far, the estimated parameter set $\hat{\boldsymbol{\Theta}}_l$ has been obtained, then iterative estimation of $\hat{\boldsymbol{\Theta}}_l$ is conducted until it converges. The parameter set $\hat{\boldsymbol{\Theta}}_l$ is updated in the order of AoA, AoD, delay, complex amplitude, birth–death coefficient of Rx, and birth–death coefficient of Tx. The detailed steps are as follows:

$$\{\hat{\boldsymbol{\Omega}}_{\text{Rx},l}^{i+1}, \hat{d}_{\text{Rx},l}^{i+1}\}$$
$$= \underset{\boldsymbol{\Omega}_{\text{Rx},l}, d_{\text{Rx},l}}{\arg\max} \{z(\boldsymbol{f}; \{\hat{\boldsymbol{\zeta}}_{\text{Rx}l}^i, \hat{\boldsymbol{\zeta}}_{\text{Tx}l}^i, \boldsymbol{\Omega}_{\text{Tx},l}^i, \hat{d}_{\text{Tx},l}^i, \hat{\tau}_l^i\})\}$$
(39)

$$\{\hat{\boldsymbol{\Omega}}_{\text{Tx},l}^{i+1}, \hat{d}_{\text{Tx},l}^{i+1}\}$$
$$= \underset{\boldsymbol{\Omega}_{\text{Tx},l}, d_{\text{Tx},l}}{\arg\max} \{z(\boldsymbol{f}; \{\hat{\boldsymbol{\zeta}}_{\text{Rx},l}^i, \hat{\boldsymbol{\zeta}}_{\text{Tx},l}^i, \hat{\boldsymbol{\Omega}}_{\text{Rx},l}^{i+1}, \hat{d}_{\text{Rx},l}^{i+1}, \hat{\tau}_l^i\})\}$$
(40)

$$\hat{\tau}_l^{i+1}$$
$$= \underset{\tau_l}{\arg\max} \{z(\boldsymbol{f}; \{\hat{\boldsymbol{\zeta}}_{\text{Rx},l}^i, \hat{\boldsymbol{\zeta}}_{\text{Tx},l}^i, \hat{\boldsymbol{\Omega}}_{\text{Rx},l}^{i+1}, \hat{\boldsymbol{\Omega}}_{\text{Tx},l}^{i+1}, \hat{d}_{\text{Rx},l}^{i+1}, \hat{d}_{\text{Tx},l}^{i+1}\})\}$$
(41)

$$\hat{\boldsymbol{\alpha}}_l^{i+1} = \sum_{k=1}^{K} \frac{1}{K} \mathbf{G}(\hat{\mathbf{C}}_{\text{Rx},k,l}, \hat{\mathbf{C}}_{\text{Tx},k,l})^{-1}$$
$$\cdot \boldsymbol{g}(f_k; \hat{\boldsymbol{\zeta}}_{\text{Rx},l}^i, \hat{\boldsymbol{\zeta}}_{\text{Tx},l}^i, \hat{\boldsymbol{\Omega}}_{\text{Rx},l}^{i+1}, \hat{\boldsymbol{\Omega}}_{\text{Tx},l}^{i+1}, \hat{d}_{\text{Rx},l}^{i+1}, \hat{d}_{\text{Tx},l}^{i+1}, \hat{\tau}_l^{i+1})$$
(42)

$$\hat{\zeta}_{\text{Rx},m,l}^{i+1} = \underset{\zeta_{\text{Rx},m,l} \in \{0,1\}}{\arg\min} \left\| \text{vec}\{\mathbf{Y}_{m,:,l}(\boldsymbol{f})\} \right.$$
$$- \text{vec}\{\mathbf{H}_{m,:}(\boldsymbol{f}; \hat{\boldsymbol{\zeta}}_{\text{Tx},l}^i, \hat{\boldsymbol{\alpha}}_l^{i+1}, \hat{\boldsymbol{\Omega}}_{\text{Rx},l}^{i+1},$$
$$\left. \hat{\boldsymbol{\Omega}}_{\text{Tx},l}^{i+1}, \hat{d}_{\text{Rx},l}^{i+1}, \hat{d}_{\text{Tx},l}^{i+1}, \hat{\tau}_l^{i+1})\}\zeta_{\text{Rx},m,l} \right\|^2$$
(43)

$$\hat{\zeta}_{\text{Tx},n,l}^{i+1} = \underset{\zeta_{\text{Tx},n,l} \in \{0,1\}}{\arg\min} \left\| \text{vec}\{\mathbf{Y}_{:,n,l}(\boldsymbol{f})\} \right.$$
$$- \text{vec}\{\mathbf{H}_{:,n}(\boldsymbol{f}; \hat{\boldsymbol{\zeta}}_{\text{Rx},l}^{i+1}, \hat{\boldsymbol{\alpha}}_l^{i+1}, \hat{\boldsymbol{\Omega}}_{\text{Rx},l}^{i+1},$$
$$\left. \hat{\boldsymbol{\Omega}}_{\text{Tx},l}^{i+1}, \hat{d}_{\text{Rx},l}^{i+1}, \hat{d}_{\text{Tx},l}^{i+1}, \hat{\tau}_l^{i+1})\}\zeta_{\text{Tx},n,l} \right\|^2$$
(44)

where $[\hat{\cdot}]^i$ denotes the ith iteration estimation results of the given argument, and the first estimated $\hat{\boldsymbol{\Theta}}_l$ is expressed as $\hat{\boldsymbol{\Theta}}_l^1$.

4) MPCs' Sifting: Since the actual number of MPCs in the environment is unknown, the number of MPCs is usually set as a large value in ML-based estimators to ensure that enough power can be extracted. In [15], it is considered that some of the diffuse scattering components (DSCs) are identified as specular components in ML-based estimators, resulting in a significant increase in the estimated number of MPCs. In addition, the calibration error of the channel sounder, the measurement error of the complex antenna pattern, and the mismatch between the parametric model and measurement data will create serious fake paths during estimation [17], which leads to the artificial spread of MPCs in the angular and delay domain. To solve the above problems, the Akaike information criterion (AIC) [15], [41] is used here to determine the appropriate number of MPCs $\hat{L}$, which can be obtained by minimizing the following equation:

$$\hat{L} = \underset{L}{\arg\min} \{-2\Lambda(\hat{\boldsymbol{\Theta}}; \mathbf{Y}(\boldsymbol{f})) + \gamma L\}$$
(45)

where $\Lambda(\hat{\boldsymbol{\Theta}}; \mathbf{Y}(\boldsymbol{f}))$ represents the log-likelihood of $\hat{\boldsymbol{\Theta}}$ in (17), and γ is a coefficient that can be adjusted to define the degree of penalty for overfitting. For convenience, let us denote $-2\Lambda(\hat{\boldsymbol{\Theta}}; \mathbf{Y}(\boldsymbol{f})) + \gamma L$ as $\eta(L)$. By substituting (17) into (45), $\eta(L)$ can be expressed by [15]

$$\eta(L) = 2\ln \pi\sigma_n^2 + \gamma L + \frac{2}{\sigma_n^2 MNK}$$
$$\times \left\| \text{vec}\{\mathbf{Y}(\boldsymbol{f})\} - \text{vec}\left\{ \sum_{l=1}^{L} \mathbf{H}(\boldsymbol{f}; \hat{\boldsymbol{\Theta}}_l) \right\} \right\|^2.$$
(46)

In [15], all the MPCs were extracted based on the wideband near-field model, then the weak MPCs were deleted by finding the minimum value of $\eta(L)$. However, this method can only remove the unreliable estimation results and cannot suppress

the influence of artificial paths in parameter estimation. In this algorithm, the value of $\eta(l)$ is calculated for each new estimated parameter set $\hat{\boldsymbol{\Theta}}_l$ and then $\eta(l) - \eta(l-1)$ is obtained by [15]

$$
\begin{aligned}
&\eta(l) - \eta(l-1)\\
&= \gamma + \frac{2}{\sigma_n^2 MNK}\left\|\text{vec}\{\mathbf{Y}(\boldsymbol{f})\} - \text{vec}\left\{\sum_{l'=1}^{l}\mathbf{H}(\boldsymbol{f};\hat{\boldsymbol{\Theta}}_{l'})\right\}\right\|^2\\
&\quad - \frac{2}{\sigma_n^2 MNK}\left\|\text{vec}\{\mathbf{Y}(\boldsymbol{f})\} - \text{vec}\left\{\sum_{l'=1}^{l-1}\mathbf{H}(\boldsymbol{f};\hat{\boldsymbol{\Theta}}_{l'})\right\}\right\|^2.
\end{aligned}
$$
(47)

If different MPCs are independent of each other in the parameter domain, $\text{vec}\{\mathbf{H}(\boldsymbol{f};\hat{\boldsymbol{\Theta}}_{l'})\}$ and $\text{vec}\{\mathbf{H}(\boldsymbol{f};\hat{\boldsymbol{\Theta}}_l)\}$ can be considered orthogonal to each other when $l \neq l'$. To simplify the notation, let us denote $\eta(l) - \eta(l-1)$ as $\Delta\eta(l)$. In this case, (47) can be simplified as

$$
\Delta\eta(l) = -\frac{2}{\sigma_n^2 MNK}\left\|\text{vec}\{\mathbf{H}(\boldsymbol{f};\hat{\boldsymbol{\Theta}}_l)\}\right\|^2 + \gamma.
$$
(48)

If $\Delta\eta(l) < 0$, which is equivalent to

$$
-\frac{1}{\sigma_n^2 MNK}\left\|\text{vec}\{\mathbf{H}(\boldsymbol{f};\hat{\boldsymbol{\Theta}}_l)\}\right\|^2 < \frac{\gamma}{2}
$$
(49)

this MPC is retained, otherwise it is deleted and the delay bin that this MPC belongs to is skipped in the subsequent estimation. It means that those MPCs with a signal-to-noise ratio (SNR) below ($\gamma/2$) will be deleted. This approach not only removes unreliable estimate results but also effectively avoids the effect of artificial paths on the estimation of the remaining MPCs. The γ used here is 2, which corresponds to the threshold of 0 dB for MPC sifting, and the selected value is considered to be sufficient in MPCs' reliability assessment [15], [42]. Moreover, the array nonstationary factors introduced into the proposed algorithm may split an omnidirectional antenna array into a directional antenna array. However, the estimation of MPCs may be inaccurate in the direction with low gain of the directional antenna [43]. To ensure reliable estimation of the MPCs, those MPCs that can only be seen by a few antennas will be deleted. The threshold selected in this article is 1/2 number of the array antennas, and those MPCs which can be seen by less than 1/2 number of the Tx antennas or Rx antennas are removed. The whole procedure of the proposed SAGE-WSNSAP algorithm is summarized in Algorithm 1.

IV. MEASUREMENT CAMPAIGN

To verify the effectiveness of the proposed algorithm, the indoor 64×32 MIMO channel measurements are conducted. In this section, the details of the measurement environment and the configuration of the channel sounder are introduced.

A. System Configuration

This measurement campaign is conducted by the Keysight time-domain channel sounder, which is composed of the Tx side and Rx side. The Tx consists of a high-speed digitizer

---

Algorithm 1 Proposed SAGE-WSNSAP Algorithm for Spatial Nonstationary Wireless Channel Parameters' Estimation

---
Input: The measured CTF $\mathbf{Y}(\boldsymbol{f})$
Output: The estimated parameter set $\hat{\boldsymbol{\Theta}}$
Find $M_{f_{\text{narr}}}$ frequency points from $\boldsymbol{f}$ to form a narrowband CTF $\mathbf{Y}(\boldsymbol{f}_{\text{narr}})$.
Let $\boldsymbol{\tau}_{bin} = [0, \frac{1}{B_{\text{narr}}}, \ldots, \frac{M_{f_{\text{narr}}}}{B_{\text{narr}}}]^T$;
Let $l = 1$;
Let $\hat{\boldsymbol{\Theta}}$ be an empty set;
while $\boldsymbol{\tau}_{bin}$ is not empty
    Parameter coarse search:
        Obtain $\hat{\boldsymbol{\Theta}}_l^{\text{init}} = \{\hat{\boldsymbol{\Omega}}_{\text{Rx},l}^{\text{init}}, \hat{\boldsymbol{\Omega}}_{\text{Tx},l}^{\text{init}}, \hat{\tau}_l^{\text{init}}\}$; // (28)–(32).
    Parameter refinement:
        Obtain $\hat{\boldsymbol{\Theta}}_l = \{\hat{\boldsymbol{\alpha}}_l, \hat{\boldsymbol{\Omega}}_{\text{Rx},l}, \hat{\boldsymbol{\Omega}}_{\text{Tx},l}, \hat{d}_{\text{Rx},l}, \hat{d}_{\text{Tx},l}, \hat{\tau}_l\}$; // (33)–(36).
    MPCs birth–death recognition:
        Let $i = 1$;
        Obtain $\hat{\boldsymbol{\Theta}}_l^i = \{\hat{\boldsymbol{\zeta}}_{\text{Rx},l}, \hat{\boldsymbol{\zeta}}_{\text{Tx},l}, \hat{\boldsymbol{\alpha}}_l, \hat{\boldsymbol{\Omega}}_{\text{Rx},l}, \hat{\boldsymbol{\Omega}}_{\text{Tx},l}, \hat{d}_{\text{Rx},l}, \hat{d}_{\text{Tx},l}, \hat{\tau}_l\}$; // (37)–(38).
        if $i = 1$ or $\hat{\boldsymbol{\Theta}}_l^i$ does not converge
            $\hat{\boldsymbol{\Theta}}_l^{i+1} \leftarrow \hat{\boldsymbol{\Theta}}_l^i$; // (40)–(44)
            $i = i + 1$;
        else
            $\hat{\boldsymbol{\Theta}}_l = \hat{\boldsymbol{\Theta}}_l^{i+1}$
        end
    SIC:
        $\hat{\boldsymbol{\Theta}} = \{\hat{\boldsymbol{\Theta}}; \hat{\boldsymbol{\Theta}}_l\}$;
        Obtain $\mathbf{Y}_l(\boldsymbol{f})$ from (20).
        Obtain $\mathbf{Y}_l(\boldsymbol{f}_{\text{narr}})$.
    MPCs' sifting:
        if $\eta(l) - \eta(l-1) < 0$ // (47)
            $l = l + 1$;
            if number of death antennas $\hat{\boldsymbol{\zeta}}_{\text{Rx},l} > M/2$ or $\hat{\boldsymbol{\zeta}}_{\text{Tx},l} > N/2$
                $l = l - 1$;
            end
        else
            Delete the delay bin from $\boldsymbol{\tau}_{bin}$.
        end
end

M8190A, a power amplifier, a 32-channel high-speed solid-state switch, and a GPS Rubidium clock. The Rx includes a wideband digital receiver M9703B, eight intermediate frequency (IF) amplifiers, an analog signal generator N5173B, a 64-channel high-speed solid-state switch, and eight mixers. The Tx side and Rx side are synchronized by 1 pulse per second (1 PPS) signal generated by the GPS Rubidium clock. The center frequency of the transmitting signal is 5.5 GHz, and the bandwidth is 320 MHz. Besides, the transmitting waveform is pseudonoise (PN) sequence with a length of 1023. Note that the CTF can be obtained by fast Fourier transform (FFT) of the measured channel impulse response (CIR). The transmitting antenna is 4×4 dual-polarization planar antenna array, and the receiving antenna is 8×4 dual-polarization cylindrical antenna array. The detailed system configurations are summarized in Table II.
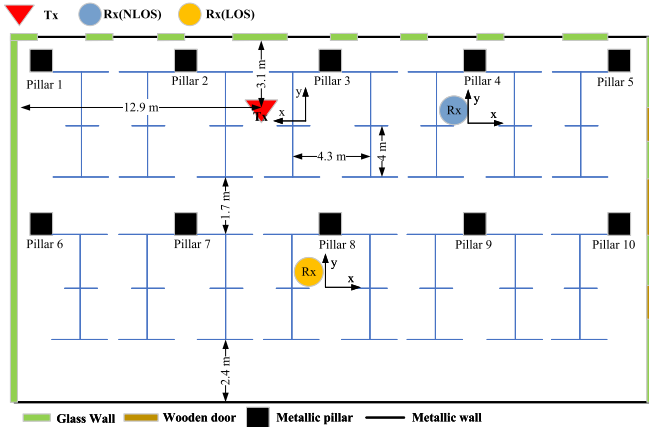
Parameters	Configurations
Frequency (GHz)	5.5
Bandwidth (MHz)	320
Delay resolution (ns)	3.125
PN code chips	1023
Tx antenna array	4×4 dual-polarization planar antenna array
Rx antenna array	8×4 dual-polarization cylindrical antenna array
Tx height (m)	3.3
Rx height (m)	1.5 (LOS), 0.75 (NLOS)

Fig. 2. Environment of the indoor office where the measurement campaign was conducted. (a) Photograph of this indoor office. (b) Layout of this indoor office environment.

B. Channel Measurement

The measurements are conducted in a typical indoor office environment, as illustrated in Fig. 2(a). There are about 100 workstations with metallic partitions and wooden boards in the office, and the heights of the partition and desk board are 1.2 and 0.75 m, respectively. There are computer monitors, mouses, and other office supplies on the desks, and the distance between the workstations is about 2 m. There are ten square metallic pillars in the office, and the surrounding walls are made of glass and metal. Both the LOS and NLOS scenarios are measured. The height of the Tx antenna array is 3.3 m, and the heights of the Rx antenna array are 1.5 and 0.75 m in the LOS and NLOS scenarios, respectively. The layout of the specific measurement scenario is shown in Fig. 2(b). The red triangle in Fig. 2(b) represents
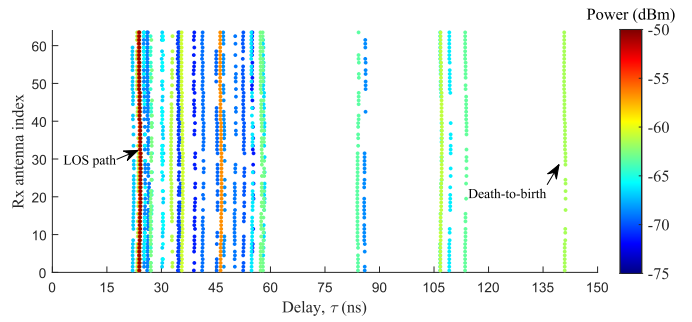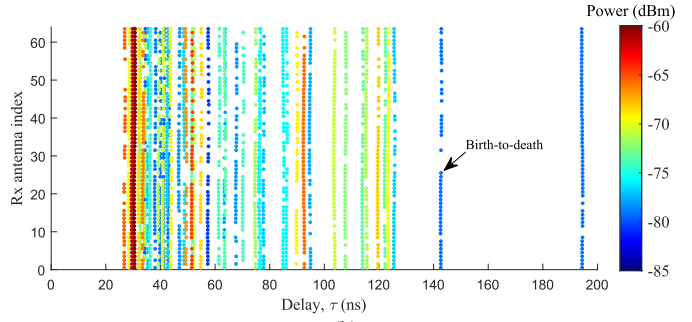
Fig. 3. Delay variation in the estimated MPCs based on the SAGE-WSNSAP algorithm at the Rx side. (a) LOS scenario. (b) NLOS scenario.

the Tx position, and the blue and yellow circles denote the Rx positions in the LOS and NLOS scenarios, respectively.

V. RESULTS AND ANALYSIS

The Rayleigh distances of the Tx and Rx antenna arrays are 0.55 and 0.82 m, respectively. Generally, the far-field assumption can be satisfied, and the far-field SAGE algorithm [38] is suitable for the parameter estimation of the measured data. However, there are abundant scatterers in the office environment, and some of them may be located within the near-field distance. The blockage brought by these near-field scatterers can cause spatial nonstationarity. Hence, the SAGE-WSNSAP algorithm may show better performance than the far-field and near-field SAGE algorithms. The parameter estimation results based on the far-field SAGE, near-field SAGE [31], and SAGE-WSNSAP algorithms are compared in this section. To ensure that most MPCs can be extracted, the initial path number is set as 150 for far-field and near-field SAGE algorithms in both the LOS and NLOS scenarios. Then the AIC in (45) is used to determine the appropriate number of MPCs, which are 45, 41, and 38 for the far-field SAGE algorithm, near-field SAGE algorithm, and SAGE-WSNSAP algorithm in the LOS scenario. In the NLOS scenario, the corresponding number of reliable MPCs extracted by these three algorithms is 69, 61, and 75, respectively.

A. Birth–Death of MPCs

Fig. 3(a) and (b) shows the delay variation in the estimated MPCs based on the proposed SAGE-WSNSAP algorithm at the Rx side in the LOS and NLOS scenarios, respectively. The powers of MPCs are distinguished by different colors,

and the same color indicates the same MPC. The estimated delay of MPCs along the Rx antenna array forms many delay tracks. The appearance and disappearance of MPCs can be seen from these delay tracks. For example, in Fig. 3(a), the green MPC delay track with a delay about 140 ns appears and disappears along the Rx antenna array, which shows the birth–death phenomenon of this estimated MPC. Compared with the number of estimated MPCs in the LOS scenario, the number of MPCs estimated in the NLOS scenario is larger. Besides, the birth–death phenomenon of the estimated MPCs in the NLOS scenario is more obvious. The reason is that there are more scatterers in the NLOS scenario, and the spatial nonstationarity caused by the blockage is more obvious. In general, the estimation results show that the proposed algorithm can identify the birth–death of MPCs along the antenna array.

B. Angle-Delay PSD

The comparisons between the measured and estimated results of the azimuth angle of arrival delay PSD (AoAD-PSD) and azimuth angle of departure delay PSD (AoDD-PSD) in the LOS scenario are shown in Figs. 4 and 5, respectively. The results show that the estimation of high-power MPCs based on these three algorithms are consistent with the measurement results, indicating that all the algorithms can accurately estimate high-power MPCs. However, those MPCs with delay larger than 100 ns are incapable of being detected by the far-field and near-field SAGE algorithms. This phenomenon is caused by the mismatch between the parametric models adopted in the traditional SAGE algorithms and the measured channels. The spatial nonstationarity was not considered in the parametric models adopted in the traditional far-field and near-field SAGE algorithms, which will bring the deviations between the estimated MPCs and the actual MPCs captured in the measured CTF $\mathbf{Y}(f)$. As a result, many fake MPCs surrounding the strong MPCs are estimated to mitigate the deviations. However, these fake MPCs with very low powers can hardly reduce the residual powers associated with the delay bins of the strong MPCs, and the residual powers are higher than the powers of MPCs located in the large delay bins. Consequently, the traditional SAGE algorithms repeatedly estimate fake MPCs around the strong MPCs, and the far-away MPCs located in large delay bins cannot be extracted with limited number of paths. However, the MPCs' sifting step in the proposed SAGE-WSNSAP algorithm will calculate the value of $\Delta\eta(l)$ after each MPC estimation. If $\Delta\eta(l) < 0$, it indicates that the SNR of this MPC is very low, and then this MPC will be deleted and the delay bin that this MPC belongs to will be skipped in the subsequent estimation. In this way, the SAGE-WSNSAP algorithm can skip those delay bins without reliable MPCs and realize the estimation of specular MPCs located in large-delay bins. In addition, it can be seen in Fig. 5 that the number of MPCs concentrated in the region around the LOS path estimated based on the far-field SAGE algorithm (13 MPCs) and near-field SAGE algorithm (11 MPCs) is more than that estimated based on the SAGE-WSNSAP algorithm (three MPCs). This phenomenon is consistent with that observed in [44]. Because the power of

the LOS path is dominant, and it will be estimated first in the CPE algorithm. However, if the transfer function reconstructed by the parametric model cannot completely eliminate the contribution of the LOS path in measured $\mathbf{Y}(f)$, fake paths will be created around the LOS path to compensate for its estimation error.
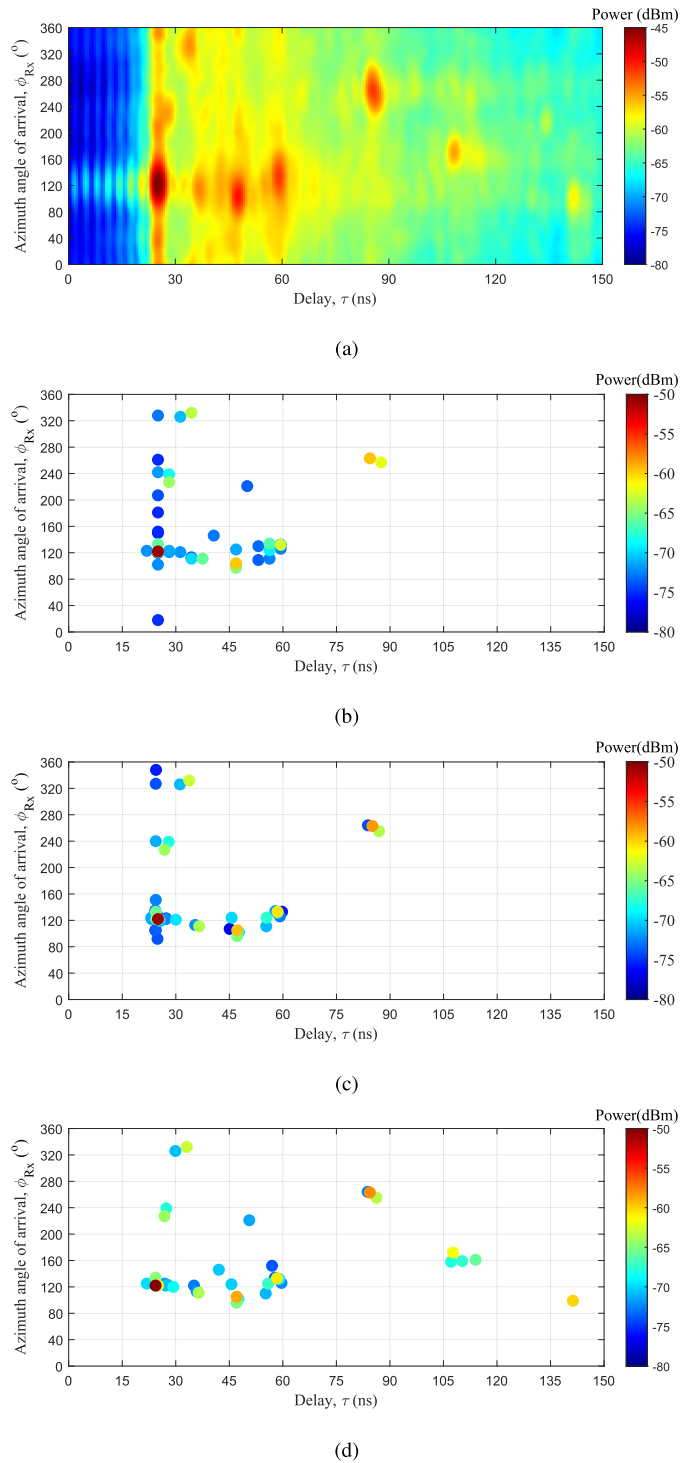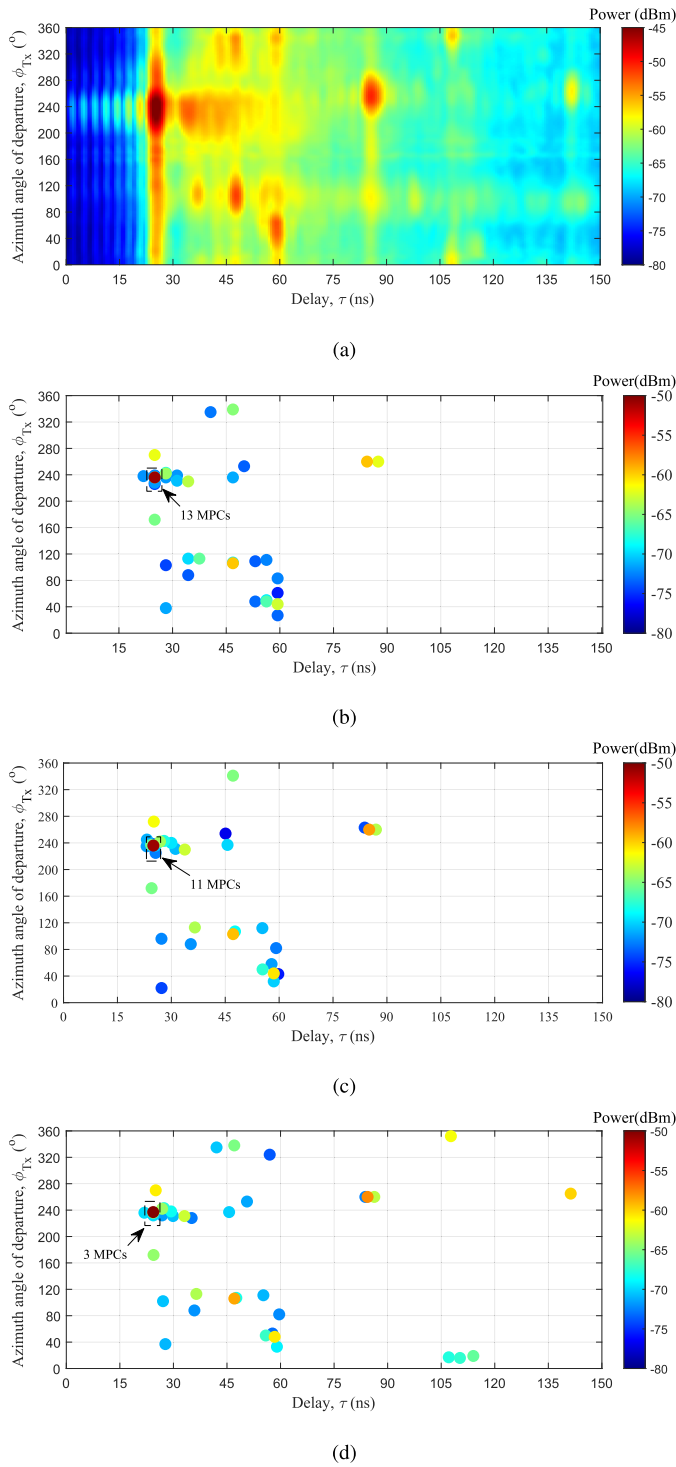

(a)

(b)

(c)

(d)

Fig. 4. AoAD-PSD results in the LOS scenario. (a) Measurement results. (b) Estimation results of the far-field SAGE algorithm. (c) Estimation results of the near-field SAGE algorithm. (d) Estimation results of the SAGE-WSNSAP algorithm.
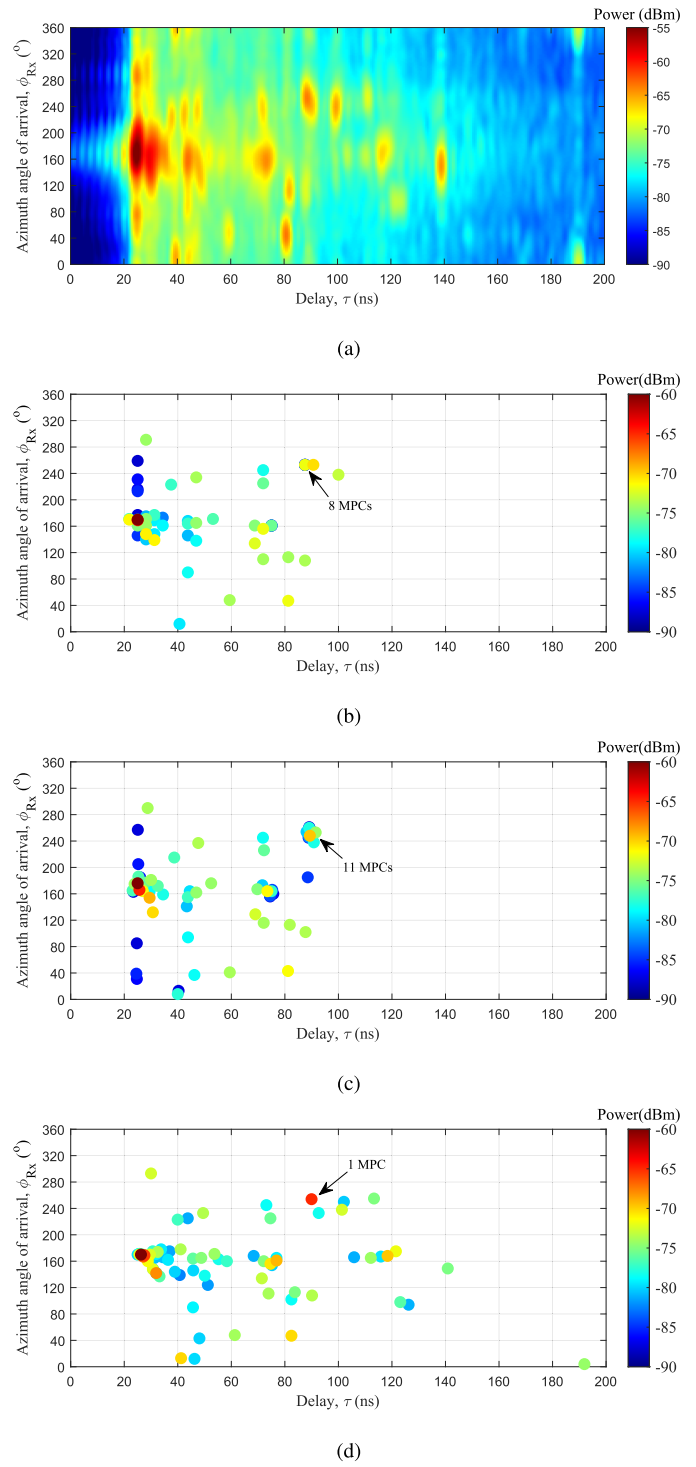
Fig. 5. AoDD-PSD results in the LOS scenario. (a) Measurement results. (b) Estimation results of the far-field SAGE algorithm. (c) Estimation results of the near-field SAGE algorithm. (d) Estimation results of the SAGE-WSNSAP algorithm.

Fig. 6. AoAD-PSD results in the NLOS scenario. (a) Measurement results. (b) Estimation results of the far-field SAGE algorithm. (c) Estimation results of the near-field SAGE algorithm. (d) Estimation results of the SAGE-WSNSAP algorithm.

Figs. 6 and 7 show the measured and estimated results of the AoAD-PSD and AoDD-PSD in the NLOS scenario. The results show that some MPCs are split into many sub-MPCs in the far-field and near-field SAGE algorithms. This is because several MPCs are estimated to form an MPC with spatial nonstationarity, when the spatial stationary signal model is

adopted. It can be seen from Fig. 7 that some MPCs estimated by the far-field and near-field SAGE algorithms do not exist in the measurement results. These fake paths are estimated due to the mismatch between the parametric model and the measurement data. Moreover, the results also show that the powers of some MPCs estimated based on the SAGE-WSNSAP
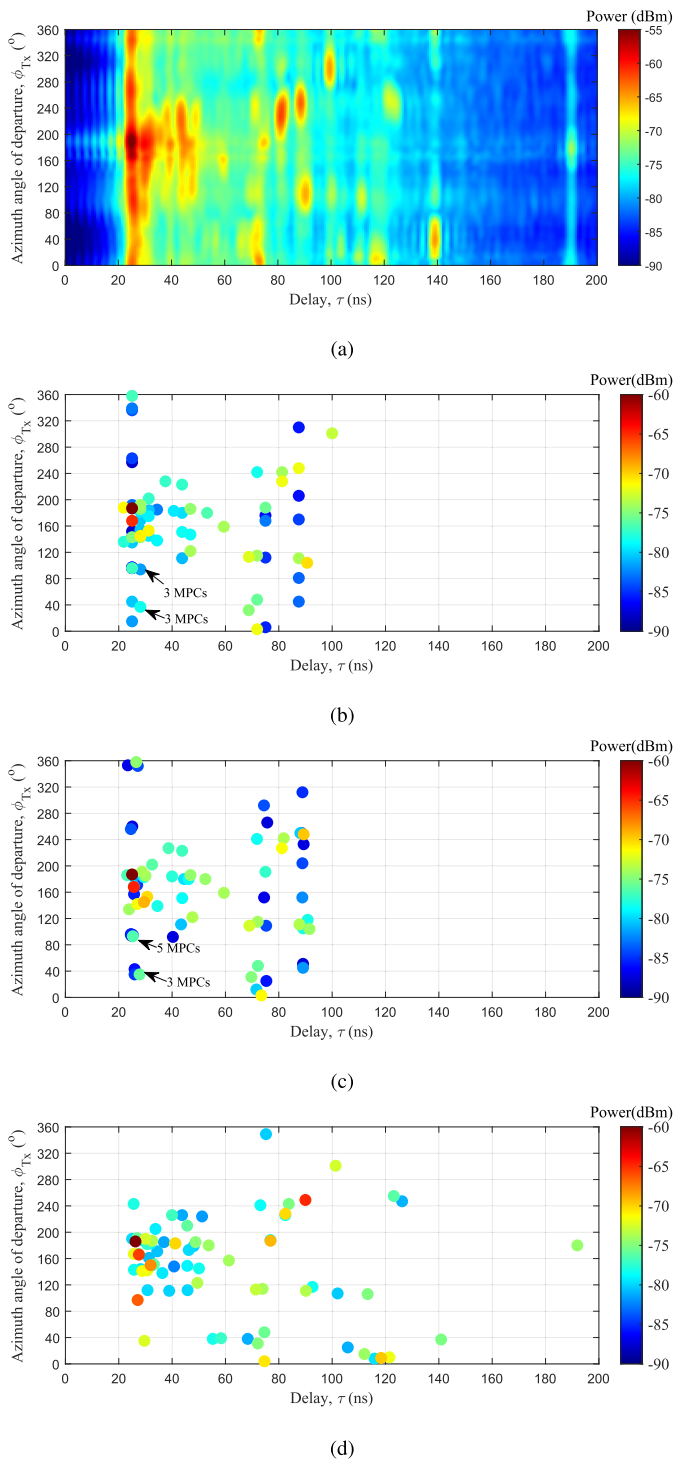
(a)

(b)

(c)

(d)

Fig. 7.　AoDD-PSD results in the NLOS scenario. (a) Measurement results. (b) Estimation results of the far-field SAGE algorithm. (c) Estimation results of the near-field SAGE algorithm. (d) Estimation results of the SAGE-WSNSAP algorithm.
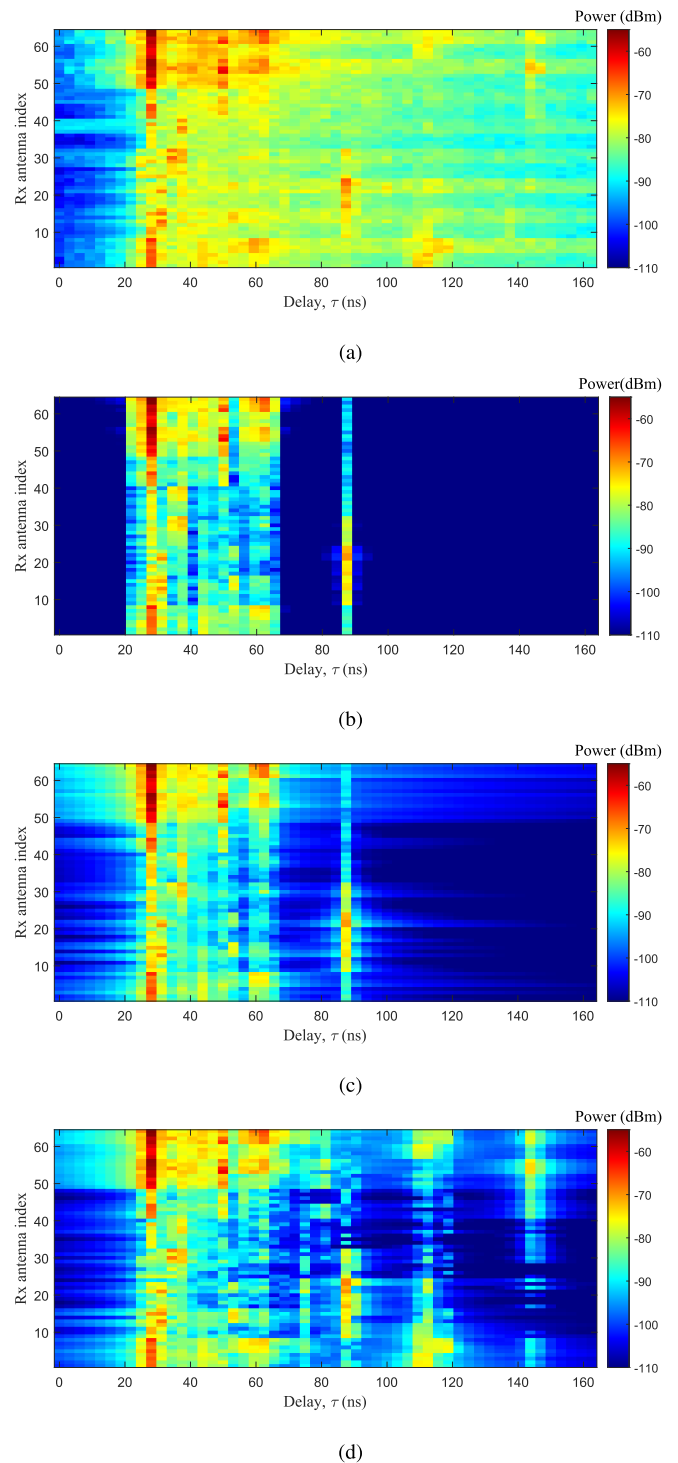

(a)

(b)

(c)

(d)

Fig. 8.　Average delay PSD of Rx in the LOS scenario. (a) Measurement results. Reconstructed average delay PSD based on (b) far-field SAGE algorithm, (c) near-field SAGE algorithm, and (d) SAGE-WSNSAP algorithm.

algorithm are slightly higher than that estimated based on the other two algorithms. Because these MPCs experience obvious spatial nonstationarity, and the estimated power will be reduced based on the spatial stationary signal model. Besides, it can be found that far-field and near-field SAGE algorithms ignore more MPCs in the NLOS scenario than in

the LOS scenario. This is due to the fact that the NLOS scenario exhibits more obvious spatial nonstationarity. Through the analysis of the estimation results shown in Figs. 4–7, it can be found that the angle-delay PSD estimated by the SAGE-WSNSAP algorithm shows higher similarity with the measured results, compared with that estimated by the far-field and near-field SAGE algorithms.
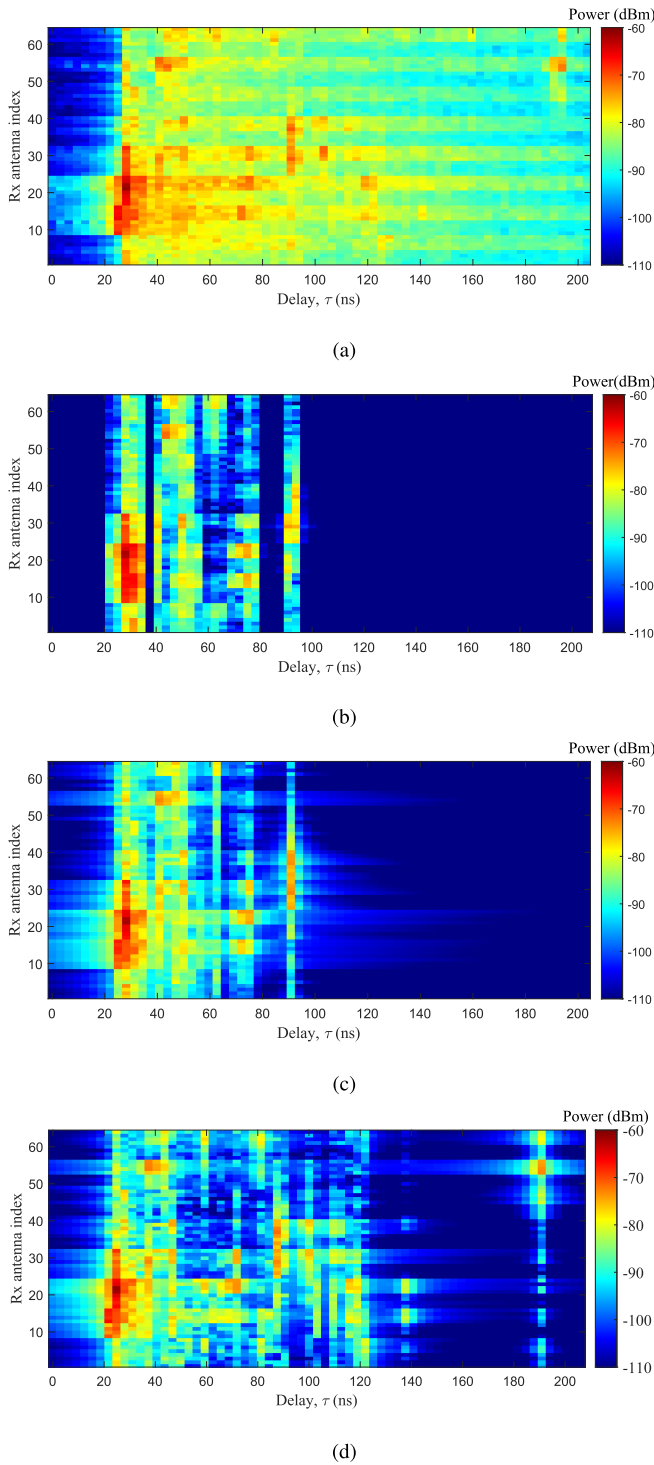
(a)

(b)

(c)

(d)

Fig. 9. Average delay PSD of Rx in the NLOS scenario. (a) Measurement results. Reconstructed average delay PSD based on (b) far-field SAGE algorithm, (c) near-field SAGE algorithm., and (d) SAGE-WSNSAP algorithm.

C. Average Delay PSD

The average delay PSD of the Rx obtained by measurements and these three algorithms in the LOS and NLOS scenarios is shown in Figs. 8 and 9, respectively. It can be observed that the powers of MPCs fluctuate significantly along the array axis, and some MPCs can only be seen by part of the antenna array.

The resulting average delay PSD from the SAGE-WSNSAP algorithm matches that from the measurements very well, whereas using the far-field and near-field SAGE algorithms ignores many weak MPCs. In addition, this article compares the power extraction ratios from the measured CTF by these three algorithms. The power extraction ratios of the far-field SAGE, near-field SAGE, and SAGE-WSNSAP algorithms are 64%, 66%, and 70% in the LOS scenario, respectively. The corresponding power extraction ratios are 46%, 49%, and 56% in the NLOS scenario. Note that a higher power extraction proportion from the measurement data means that more effective MPCs' information can be estimated. In the LOS scenario, the power of the LOS path dominates, so more power can be extracted. In the NLOS scenario, the richer scatterers and more obvious spatial nonstationarity contribute to a larger performance difference between the SAGE-WSNSAP algorithm and the other two algorithms. Besides, the results show that the power extraction ratio difference in the far-field SAGE and near-field SAGE algorithms is small (less than 3%) in both the LOS and NLOS scenarios. Because the Rayleigh distance of the antenna array is small, and there is no significant difference between the near-field signal model and far-field signal model. By comparing the parameter estimation results of these three algorithms, as shown in Figs. 8 and 9, the proposed SAGE-WSNSAP algorithm shows the best performance in terms of power extraction ratio.

VI. CONCLUSION

In this article, a SAGE-WSNSAP algorithm for parameter estimation of wideband spatial nonstationary channels with antenna polarization has been proposed. Compared with the far-field and near-field SAGE algorithms, the proposed SAGE-WSNSAP algorithm has added spatial nonstationarity by introducing array birth–death coefficients at both the Tx and Rx sides into the parametric model. To reduce the complexity of the proposed algorithm, a coarse-to-fine search method has been adopted in the parameter initialization step. Meanwhile, those unreliable estimated MPCs have been removed in the MPCs' sifting step.

Moreover, the MIMO channel measurements in a typical indoor office environment have been conducted to validate the SAGE-WSNSAP algorithm. The estimation results of angle-delay PSD and average delay PSD obtained by the far-field SAGE, near-field SAGE, and SAGE-WSNSAP algorithms have been compared with the measurement results. It has been found that the angle-delay PSD and average delay PSD estimated by the SAGE-WSNSAP algorithm show higher similarity to the measurement results, compared with those estimated by the other two SAGE algorithms. Besides, in the LOS scenario, the power extraction ratios based on the far-field SAGE, near-field SAGE, and SAGE-WSNSAP algorithms are 64%, 66%, and 70%, respectively. Similarly, in the NLOS scenario, the corresponding power extraction ratios based on these three algorithms are 46%, 49%, and 56%. It means that the proposed algorithm can extract more effective MPC powers from measurements, in both the LOS and NLOS scenarios. Due to the mismatch between the measured data and the parametric model, the far-field and near-field SAGE

algorithms present more fake MPCs around the LOS path. In addition, compared with the LOS scenario, the NLOS scenario exhibits more obvious spatial nonstationarity, which makes the SAGE-WSNSAP algorithm outperform the other two SAGE algorithms more obviously.

REFERENCES

[1] C.-X. Wang et al., "On the road to 6G: Visions, requirements, key technologies, and testbeds," *IEEE Commun. Surveys Tuts.*, vol. 25, no. 2, pp. 905–974, 2nd Quart. 2023.

[2] C.-X. Wang, Z. Lv, X.-Q. Gao, X.-H. You, Y. Hao, and H. Haas, "Pervasive wireless channel modeling theory and applications to 6G GBSMs for all frequency bands and all scenarios," *IEEE Trans. Veh. Technol.*, vol. 71, no. 9, pp. 9159–9173, Sep. 2022.

[3] C.-X. Wang, J. Huang, H. Wang, X.-Q. Gao, X.-H. You, and Y. Hao, "6G wireless channel measurements and models: Trends and challenges," *IEEE Veh. Technol. Mag.*, vol. 15, no. 4, pp. 22–32, Dec. 2020.

[4] J. A. Zhang et al., "Enabling joint communication and radar sensing in mobile networks—A survey," *IEEE Commun. Surveys Tuts.*, vol. 24, no. 1, pp. 306–345, 1st Quart., 2022.

[5] C. De Lima et al., "Convergent communication, sensing and localization in 6G systems: An overview of technologies, opportunities and challenges," *IEEE Access*, vol. 9, pp. 26902–26925, 2021.

[6] H. Alidoustaghdam, Y. Miao, and A. Kokkeler, "Integrating TDD communication and radar sensing in co-located planar array: A genetic algorithm enabled aperture design," in *Proc. 2nd IEEE Int. Symp. Joint Commun. Sens. (JC&S)*, Seefeld, Austria, Mar. 2022, pp. 1–6.

[7] M. Nakamura, M. Sasaki, M. Inomata, and Y. Takatori, "Path-loss prediction considering human-body shadowing of multi-path components in crowded area at 4.7 and 26.4 GHz," in *Proc. Int. Symp. Antennas Propag. (ISAP)*, Phuket, Thailand, Oct. 2017, pp. 1–2.

[8] R. He, B. Ai, G. L. Stüber, G. Wang, and Z. Zhong, "Geometrical-based modeling for millimeter-wave MIMO mobile-to-mobile channels," *IEEE Trans. Veh. Technol.*, vol. 67, no. 4, pp. 2848–2863, Apr. 2018.

[9] D. Tse and P. Viswanath, *Fundamentals of Wireless Communication*. Cambridge, U.K.: Cambridge Univ., 2005.

[10] K. Guan et al., "On millimeter wave and THz mobile radio channel for smart rail mobility," *IEEE Trans. Veh. Technol.*, vol. 66, no. 7, pp. 5658–5674, Jul. 2017.

[11] D. K. P. Tan et al., "Integrated sensing and communication in 6G: Motivations, use cases, requirements, challenges and future directions," in *Proc. 1st IEEE Int. Online Symp. Joint Commun. Sens. (JC&S)*, Dresden, Germany, Feb. 2021, pp. 1–6.

[12] J. Yang et al., "Integrated communication and localization in millimeter-wave systems," *Front. Inf. Technol. Electron. Eng.*, vol. 22, no. 4, pp. 457–470, Feb. 2021.

[13] H. Krim and M. Viberg, "Two decades of array signal processing research: The parametric approach," *IEEE Signal Process. Mag.*, vol. 13, no. 4, pp. 67–94, Jul. 1996.

[14] S. Zhang, T. Jost, R. Pöhlmann, A. Dammann, D. Shutin, and P. A. Hoeher, "Spherical wave positioning based on curvature of arrival by an antenna array," *IEEE Wireless Commun. Lett.*, vol. 8, no. 2, pp. 504–507, Apr. 2019.

[15] Y. Ji, W. Fan, and G. F. Pedersen, "Channel characterization for wideband large-scale antenna systems based on a low-complexity maximum likelihood estimator," *IEEE Trans. Wireless Commun.*, vol. 17, no. 9, pp. 6018–6028, Sep. 2018.

[16] R. He, B. Ai, G. L. Stüber, and Z. Zhong, "Geometrical-based statistical modeling for polarized MIMO mobile-to-mobile channels," *IEEE Trans. Antennas Propag.*, vol. 66, no. 8, pp. 4213–4227, Aug. 2018.

[17] M. Landmann, M. Kaske, and R. S. Thoma, "Impact of incomplete and inaccurate data models on high resolution parameter estimation in multidimensional channel sounding," *IEEE Trans. Antennas Propag.*, vol. 60, no. 2, pp. 557–573, Feb. 2012.

[18] J. Chen, X. Yin, X. Cai, and S. Wang, "Measurement-based massive MIMO channel modeling for outdoor LoS and NLoS environments," *IEEE Access*, vol. 5, pp. 2126–2140, 2017.

[19] J. Li et al., "The 3D spatial non-stationarity and spherical wavefront in massive MIMO channel measurement," in *Proc. 10th Int. Conf. Wireless Commun. Signal Process. (WCSP)*, Hangzhou, China, Oct. 2018, pp. 1–6.

[20] S. Payami and F. Tufvesson, "Channel measurements and analysis for very large array systems at 2.6 GHz," in *Proc. 6th Eur. Conf. Antennas Propag. (EUCAP)*, Prague, Czech Republic, Mar. 2012, pp. 433–437.

[21] R. Feng, J. Huang, J. Sun, and C.-X. Wang, "A novel 3D frequency domain SAGE algorithm with applications to parameter estimation in mmWave massive MIMO indoor channels," *Sci. China Inf. Sci.*, vol. 60, no. 8, Aug. 2017, Art. no. 080305, doi: 10.1007/s11432-017-9139-4.

[22] M. S. Bartlett, "Smoothing periodograms from time-series with continuous spectra," *Nature*, vol. 161, no. 4096, pp. 686–687, May 1948.

[23] J. Capon, "High-resolution frequency-wavenumber spectrum analysis," *Proc. IEEE*, vol. 57, no. 8, pp. 1408–1418, Aug. 1969.

[24] J. Zhang and M. Haardt, "Channel estimation for hybrid multi-carrier mmWave MIMO systems using three-dimensional unitary esprit in DFT beamspace," in *Proc. IEEE 7th Int. Workshop Comput. Adv. Multi-Sensor Adapt. Process. (CAMSAP)*, Curacao, The Netherlands, Dec. 2017, pp. 1–5.

[25] Z. Guo, X. Wang, and W. Heng, "Millimeter-wave channel estimation based on 2-D beamspace MUSIC method," *IEEE Trans. Wireless Commun.*, vol. 16, no. 8, pp. 5384–5394, Aug. 2017.

[26] Z. Ma, D. He, X. Chen, and W. Yu, "Localization of 3-D near-field sources based on the joint phase interferometer and MUSIC algorithm," in *Proc. IEEE Globecom Workshops (GC Wkshps)*, Taipei, Taiwan, Dec. 2020, pp. 1–6.

[27] X. Zhang, W. Chen, W. Zheng, Z. Xia, and Y. Wang, "Localization of near-field sources: A reduced-dimension MUSIC algorithm," *IEEE Commun. Lett.*, vol. 22, no. 7, pp. 1422–1425, Jul. 2018.

[28] A. Ritcher, M. Landmann, and R. S. Thoma, "Maximum likelihood channel parameter estimation from multidimensional channel sounding measurements," in *Proc. 57th IEEE Semiannual Veh. Technol. Conf.*, Jeju, Korea (South), Jul. 2003, pp. 1056–1060.

[29] T. K. Moon, "The expectation-maximization algorithm," *IEEE Signal Process. Mag.*, vol. 13, no. 6, pp. 47–60, Nov. 1996.

[30] B. H. Fleury, M. Tschudin, R. Heddergott, D. Dahlhaus, and K. I. Pedersen, "Channel parameter estimation in mobile radio environments using the SAGE algorithm," *IEEE J. Sel. Areas Commun.*, vol. 17, no. 3, pp. 434–450, Mar. 1999.

[31] X. Yin, S. Wang, N. Zhang, and B. Ai, "Scatterer localization using large-scale antenna arrays based on a spherical wave-front parametric model," *IEEE Trans. Wireless Commun.*, vol. 16, no. 10, pp. 6543–6556, Oct. 2017.

[32] J. Wang et al., "A novel 3D non-stationary GBSM for 6G THz ultra-massive MIMO wireless systems," *IEEE Trans. Veh. Technol.*, vol. 70, no. 12, pp. 12312–12324, Dec. 2021.

[33] J. Bian, C.-X. Wang, X. Gao, X.-H. You, and M. Zhang, "A general 3D non-stationary wireless channel model for 5G and beyond," *IEEE Trans. Wireless Commun.*, vol. 20, no. 5, pp. 3211–3224, May 2021.

[34] X. Cai and W. Fan, "A complexity-efficient high resolution propagation parameter estimation algorithm for ultra-wideband large-scale uniform circular array," *IEEE Trans. Commun.*, vol. 67, no. 8, pp. 5862–5874, Aug. 2019.

[35] X. Cai, W. Fan, X. Yin, and G. F. Pedersen, "Trajectory-aided maximum-likelihood algorithm for channel parameter estimation in ultrawideband large-scale arrays," *IEEE Trans. Antennas Propag.*, vol. 68, no. 10, pp. 7131–7143, Oct. 2020.

[36] J. Huang, C. Wang, R. Feng, J. Sun, W. Zhang, and Y. Yang, "Multi-frequency mmWave massive MIMO channel measurements and characterization for 5G wireless communication systems," *IEEE J. Sel. Areas Commun.*, vol. 35, no. 7, pp. 1591–1605, Jul. 2017.

[37] Y. Zheng, C.-X. Wang, J. Huang, R. Feng, and J. Thompson, "Measurements and characteristics analysis of 6 G ultra-massive MIMO wireless channels with different antenna configurations and scenarios," *IEEE Trans. Veh. Technol.*, early access, Mar. 17, 2023, doi: 10.1109/TVT.2023.3258456.

[38] X. Yin, B. H. Fleury, P. Jourdan, and A. Stucki, "Polarization estimation of individual propagation paths using the SAGE algorithm," in *Proc. 14th IEEE Pers., Indoor Mobile Radio Commun. (PIMRC)*, Beijing, China, Sep. 2003, pp. 1795–1799.

[39] J. A. Fessler and A. O. Hero, "Space-alternating generalized expectation-maximization algorithm," *IEEE Trans. Signal Process.*, vol. 42, no. 10, pp. 2664–2677, Oct. 1994.

[40] X. Yin and X. Cheng, *Propagation Channel Characterization, Parameter Estimation, and Modeling for Wireless Communications*. Hoboken, NJ, USA: Wiley, 2016.

[41] H. Akaike, "A new look at the statistical model identification," *IEEE Trans. Autom. Control*, vol. AC-19, no. 6, pp. 716–723, Dec. 1974.

[42] R. He, Z. Zhong, B. Ai, J. Ding, Y. Yang, and A. F. Molisch, "Short-term fading behavior in high-speed railway cutting scenario: Measurements, analysis, and statistical models," *IEEE Trans. Antennas Propag.*, vol. 61, no. 4, pp. 2209–2222, Apr. 2013.

[43] X. Yin, Y. Hu, and Z. Zhong, "Dynamic range selection for antenna-array gains in high-resolution channel parameter estimation," in *Proc. Int. Conf. Wireless Commun. Signal Process.*, Huangshan, China, Oct. 2012, pp. 1–6.

[44] Y. Ji, W. Fan, and G. F. Pedersen, "Near-field signal model for large-scale uniform circular array and its experimental validation," *IEEE Antennas Wireless Propag. Lett.*, vol. 16, pp. 1237–1240, 2017.

International Wireless Communications and Mobile Computing Conference (IWCMC) 2015, IWCMC 2016, IEEE/CIC International Conference on Communications in China (ICCC) 2016, International Symposium on Wireless Personal Multimedia Communications (WPMC) 2016, Wireless and Optical Communications Conference (WOCC) 2019, IWCMC 2020, International Conference on Wireless Communications and Signal Processing (WCSP) 2020, International Conference on Communications, Signal Processing, and Systems (CSPS) 2021, WCSP 2021, and IEEE/CIC ICCC 2022. He has served as a TPC member, the TPC Chair, and the General Chair for more than 30 international conferences. He has served as an Editor for more than ten international journals, including the IEEE TRANSACTIONS ON WIRELESS COMMUNICATIONS from 2007 to 2009, the IEEE TRANSACTIONS ON VEHICULAR TECHNOLOGY from 2011 to 2017, and the IEEE TRANSACTIONS ON COMMUNICATIONS from 2015 to 2017. He was a Guest Editor of the IEEE JOURNAL ON SELECTED AREAS IN COMMUNICATIONS, Special Issue on Vehicular Communications and Networks (Lead Guest Editor), Special Issue on Spectrum and Energy Efficient Design of Wireless Communication Networks, and Special Issue on Airborne Communication Networks. He was also a Guest Editor for the Special Issue on Wireless Big Data of the IEEE TRANSACTIONS ON BIG DATA. He is an Executive Editorial Committee Member of the IEEE TRANSACTIONS ON WIRELESS COMMUNICATIONS. He is also a Guest Editor for the Special Issue on Intelligent Resource Management for 5G and Beyond for the IEEE TRANSACTIONS ON COGNITIVE COMMUNICATIONS AND NETWORKING.

Zihao Zhou (Student Member, IEEE) received the B.E. degree from the Nanjing University of Posts and Telecommunications, Nanjing, China, in 2019. He is currently pursuing the Ph.D. degree with the National Mobile Communications Research Laboratory, Southeast University, Nanjing.

His research interests include channel parameter estimation and multifrequency channel measurements, characteristics analysis, and modeling.

Li Zhang (Student Member, IEEE) received the B.E. degree from Hunan University, Changsha, China, in 2019. She is currently pursuing the Ph.D. degree with the National Mobile Communications Research Laboratory, Southeast University, Nanjing, China.

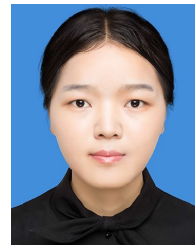Her research interests include indoor channel measurements, characteristics analysis, and modeling.

Cheng-Xiang Wang (Fellow, IEEE) received the B.Sc. and M.Eng. degrees in communication and information systems from Shandong University, Jinan, China, in 1997 and 2000, respectively, and the Ph.D. degree in wireless communications from Aalborg University, Aalborg, Denmark, in 2004.

He was a Research Assistant with the Hamburg University of Technology, Hamburg, Germany, from 2000 to 2001; a Visiting Researcher with Siemens AG Mobile Phones, Munich, Germany, in 2004; and a Research Fellow with the University of Agder, Grimstad, Norway, from 2001 to 2005. He has been with Heriot-Watt University, Edinburgh, U.K., since 2005, where he was promoted to a Professor in 2011. In 2018, he joined Southeast University, Nanjing, China, as a Professor. He is also a part-time Professor with Purple Mountain Laboratories, Nanjing. He has authored four books, three book chapters, and more than 500 papers in refereed journals and conference proceedings, including 27 highly cited papers. He has also delivered 24 invited keynote speeches/talks and 16 tutorials in international conferences. His current research interests include wireless channel measurements and modeling, 6G wireless communication networks, and electromagnetic information theory.

Dr. Wang is a member of the Academia Europaea (The Academy of Europe) and the European Academy of Sciences and Arts (EASA); a fellow of the Royal Society of Edinburgh (FRSE), IET, and the China Institute of Communications (CIC); an IEEE Communications Society Distinguished Lecturer in 2019 and 2020; a Highly Cited Researcher recognized by Clarivate Analytics from 2017 to 2020. He has received 15 Best Paper Awards from IEEE Global Communications Conference (GLOBECOM) 2010, IEEE International Conference on Communication Technology (ICCT) 2011, International Conference on Intelligent Transport System Telecommunications (ITST) 2012, IEEE Vehicular Technology Conference (VTC)-Spring 2013,

Jie Huang (Member, IEEE) received the B.E. degree in information engineering from Xidian University, Xi'an, China, in 2013, and the Ph.D. degree in information and communication engineering from Shandong University, Jinan, China, in 2018.

From October 2018 to October 2020, he was a Post-Doctoral Research Associate with the National Mobile Communications Research Laboratory, Southeast University, Nanjing, China, supported by the National Postdoctoral Program for Innovative Talents, where he has been an Associate Professor since November 2020. From January 2019 to February 2020, he was a Post-Doctoral Research Associate with Durham University, Durham, U.K. Since March 2019, he has been a part-time Researcher with the Purple Mountain Laboratories, Nanjing. He has authored and coauthored more than 70 papers in refereed journals and conference proceedings. His research interests include millimeter-wave, massive multiple-input–multiple-output (MIMO), reconfigurable intelligent surface channel measurements and modeling, wireless big data, and 6G wireless communications.

Dr. Huang has received the Best Paper Awards from International Symposium on Wireless Personal Multimedia Communications (WPMC) 2016, International Conference on Wireless Communications and Signal Processing (WCSP) 2020 and WCSP 2021. He has delivered nine tutorials in IEEE/China Institute of Communications (CIC) International Conference on Communications in China (ICCC) 2021, IEEE International Symposium on Personal Indoor and Mobile Radio Communications (PIMRC) 2021, IEEE International Conference on Communications (ICC) 2022, IEEE Vehicular Technology Conference (VTC)-Spring 2022, IEEE/CIC ICCC 2022, IEEE VTC-Fall 2022, IEEE PIMRC 2022, IEEE Global Communications Conference (GLOBECOM) 2022, and IEEE WCNC 2023..

Lijian Xin (Member, IEEE) received the Ph.D. degree from the Beijing University of Posts and Telecommunications (BUPT), Beijing, China, in 2021.

He is currently with Purple Mountain Laboratories, Nanjing, China, as an Assistant Research Fellow. His main areas of research interests include over-the-air (OTA) testing of massive multiple-input–multiple-output (MIMO) devices, channel measurement, and modeling.

El-Hadi M. Aggoune (Life Senior Member, IEEE) received the M.Sc. and Ph.D. degrees in electrical engineering from the University of Washington (UW), Seattle, WA, USA, in 1984 and 1988, respectively.

He has served at several universities in USA and abroad at many academic ranks, including Endowed Chair Professor. He is currently serving as a Professor and the Director of the Sensor Networks and Cellular Systems (SNCS) Research Center, University of Tabuk, Tabuk, Saudi Arabia. His research interests include wireless communication, sensor networks, power systems, neurocomputing, and scientific visualization.

Dr. Aggoune is listed as an Inventor in several patents, one of them assigned to Boeing Company, USA. He is a Professional Engineer registered in the state of Washington. He has coauthored papers in IEEE and other journals and conferences, and served on editorial boards and technical committees for many of them. He was a recipient of the IEEE Professor of the Year Award, UW. He was the Director of a laboratory that received the Boeing Supplier Excellence Award.
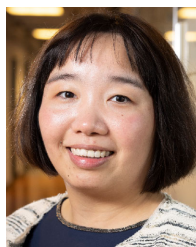
Yang Miao (Member, IEEE) received the M.Sc. and Ph.D. degrees from the Radio Propagation Laboratory, Mobile Communications Research Group, Tokyo Institute of Technology, Tokyo, Japan, in 2012 and 2015, respectively.

From 2010 to 2015, she was a Research Assistant with the Takada Laboratory, Tokyo Institute of Technology. From 2015 to 2018, she was a Post-Doctoral Researcher with the Institute of Information and Communication Technologies, Electronics, and Applied Mathematics, Universite Catholique de Louvain, Louvain-la-Neuve, Belgium, and IMEC, Wireless, Acoustics, Environment, and the Expert Systems Laboratory, Ghent University, Ghent, Belgium. From 2017 to 2018, she was a part-time Senior Antenna Engineer with Jaguar Radio Wave Corporation, Shenzhen, China. From 2018 to 2019, she was a Research Assistant Professor with the Southern University of Science and Technology, Shenzhen, China. Since August 2019, she has been an Assistant Professor with the Radio Systems Group, University of Twente, Enschede, The Netherlands. Since November 2021, she has been affiliated in part-time at Katholieke Universiteit (KU) Leuven, Leuven, Belgium, as a Marie Curie Individual Fellow. Her current research interests include joint communication and sensing, incorporating mobility, and human factors.